

# Ejecta distribution and momentum transfer from oblique impacts on asteroid surfaces

S. D. Raducan<sup>1, 2</sup>, T. M. Davison<sup>1</sup>, and G. S. Collins<sup>1</sup>

<sup>1</sup>Impacts and Astromaterials Research Centre, Department of Earth Science  
and Engineering, Imperial College London, United Kingdom.

<sup>2</sup>Space Research and Planetary Sciences, Physikalisches Institut, University  
of Bern, Switzerland;

## Abstract

NASA’s Double Asteroid Redirection Test (DART) mission will impact its target asteroid, Dimorphos, at an oblique angle that will not be known prior to the impact. We computed iSALE-3D simulations of DART-like impacts on asteroid surfaces at different impact angles and found that the vertical momentum transfer efficiency,  $\beta$ , is similar for different impact angles, however, the imparted momentum is reduced as the impact angle decreases. It is expected that the momentum imparted from a  $45^\circ$  impact is reduced by up to 50% compared to a vertical impact. The direction of the ejected momentum is not normal to the surface, however it is observed to ‘straighten up’ with crater growth. iSALE-2D simulations of vertical impacts provide context for the iSALE-3D simulation results and show that the ejection angle varies with both target properties and with crater growth. While the ejection angle is relatively insensitive to the target porosity, it varies by up to  $30^\circ$  with target coefficient of internal friction. The simulation results presented in this paper can help constrain target properties from

the DART crater ejecta cone, which will be imaged by the LICIACube. The results presented here represent the basis for an empirical scaling relationship for oblique impacts and can be used as a framework to determine an analytical approximation of the vertical component of the ejecta momentum,  $\beta - 1$ , given known target properties.

## 1 Introduction

NASA’s Double Asteroid Redirection Test (DART) will be the first mission to test a controlled deflection of a Near-Earth binary asteroid (Cheng et al., 2016; Michel et al., 2016), by impacting the smaller component of the 65803 Didymos asteroid system, Dimorphos. The impact will thereby alter the binary orbit period by an amount detectable from Earth (Cheng et al., 2018). ESA’s Hera mission (Cheng et al., 2018; Michel et al., 2018) will arrive at Dimorphos several years after the DART impact, rendezvous with the asteroid system and perform detailed characterisation of Dimorphos and the DART impact outcome. Hera will determine the target’s volume and surface properties, as well as the volume and morphology of the DART impact crater and the post-impact dynamical state of the Didymos system.

In a high-velocity, head-on impact between a spacecraft and an asteroid, the change in momentum of the asteroid,  $\Delta P$ , can be amplified by the momentum of crater ejecta that exceeds the asteroid’s escape velocity. The total momentum change to the asteroid divided by the impactor momentum is a measure of deflection efficiency, commonly defined as  $\beta = \Delta P / (mU)$ , where  $mU$  is the impactor momentum.  $\beta = 1$  implies that the crater ejecta makes a negligible contribution to the total momentum change, while  $\beta > 2$  means that the momentum contribution from the crater ejecta is larger than the momentum imparted by the impactor directly. The amount by which crater ejecta enhances asteroid deflection—that is, the momentum of the crater ejecta that escapes the gravitational attraction of the target body divided by the impactor momentum ( $\beta - 1$ )—has been found to vary significantly depending on the target asteroid’s properties, composition and structure (e.g., Jutzi and Michel, 2014; Stickle et al., 2015; Syal et al., 2016; Raducan et al., 2019; Raducan et al., 2020).

These numerical studies have considered DART as a vertical impact, however, in reality, the DART spacecraft will likely impact Dimorphos’ surface at an oblique angle (Cheng et al., 2018). The exact impact angle will depend on both the spacecraft’s incoming trajectory (Atchison et al., 2016) and on the local slope of the target at the impact point. While the spacecraft’s trajectory can be computed to some degree of accuracy, the target surface morphology is not known prior to the impact.

Even though it is not yet well understood how  $\beta - 1$  is affected by the impact angle, it is expected that any departure from a vertical impact will reduce the deflection efficiency. This trend was seen previously in laboratory experiments (e.g., Yanagisawa and Hasegawa, 2000), however the effects of impact angle on momentum transfer are yet to be fully quantified. Several laboratory experiments have measured the ejection angle and ejection velocities of ejecta produced by oblique impacts (Anderson et al., 2003; Anderson et al., 2004), however such studies are difficult to conduct in laboratory and only limited data is available. The effect of impact angle on ejecta mass-velocity-launch position distributions, and its interplay with target properties, has not been systematically investigated, as this requires much more computationally demanding fully three-dimensional calculations. Numerical simulations can be used to quantify the effects of various target properties and various impact conditions on the cratering process (e.g., Prieur et al., 2017; Luther et al., 2018; Raducan et al., 2019) and inform empirical scaling laws. For example, Raducan et al. (2019) showed that empirical scaling relationships for vertical impacts (Housen and Holsapple, 2011) can be used to accurately predict momentum transfer, however equivalent scaling relationships for oblique impacts do not exist.

In this work we simulated the DART experiment as an oblique impact at four different impact angles in three dimensions. We use our simulation results to determine the net momentum transfer of the DART impact for one possible set of asteroid target properties. Our simulation results are also used to determine the radial and azimuthal variation in ejection velocity and angle for different impact angles. Together with vertical simulation results of

the radial variation in ejection velocity and angle, as a function of different target properties, these data allow us to develop a framework for integrating the effect of impact angle into existing crater ejecta scaling relationships and for estimating the deflection efficiency of an oblique impact, given known target properties and impact conditions.

## 2 Scaling of crater size and ejecta mass-velocity distribution from vertical impacts

Crater and ejecta scaling relationships are widely used to extrapolate the results of impact experiments at laboratory-scale to predict the outcome of planetary-scale events. The most widely used of these relationships are derived by approximating the impact as a point source (Holsapple and Schmidt, 1987). In this case, any outcome of an impact, such as crater size or mass-velocity distribution of the crater ejecta, is related to impactor and target properties (e.g., impactor mass, speed, target cohesion, porosity) through a so-called coupling parameter  $C \sim a\delta^\nu U^\mu$  that represents the impactor's influence on the cratering process in a single measure (Housen et al., 1983; Housen and Holsapple, 2011). In this expression,  $a$  is the impactor radius,  $\delta$  is the impactor density,  $U$  is the impactor speed and  $\nu$  and  $\mu$  are constants. The density scaling exponent  $\nu$  is often assumed to be independent of material properties, with a value of  $\approx 0.4$  (Schmidt, 1980; Housen and Holsapple, 2003). On the other hand, the velocity scaling exponent  $\mu$  depends on the target material properties (Schmidt and Housen, 1987; Prieur et al., 2017; Raducan et al., 2019) and takes values between the theoretical limits of  $\mu = 1/3$  if the coupling parameter scales with the momentum of the impactor, and  $\mu = 2/3$  if the coupling parameter scales with the impact energy (Holsapple and Schmidt, 1987).

For example, applying the coupling parameter concept to crater size, the crater radius,  $R$ , normalised by the cube root of the target density,  $\rho$ , and impactor mass,  $m$ , can be expressed in terms of the  $\pi$ -group dimensionless parameters  $\pi_2 = \frac{ga}{U^2}$ ,  $\pi_3 = \frac{Y}{\rho U^2}$  and  $\pi_4 = \frac{\rho}{\delta}$ ,

where  $g$  is the target gravity and  $Y$  is a measure of target strength. If crater growth is halted principally by the target strength, then crater formation is said to occur in the ‘strength’ regime. In this case, crater radius is independent of  $\pi_2$  and the scaling relationship takes the form:

$$R \left( \frac{\rho}{m} \right)^{1/3} = H_2 \left( \frac{Y}{\rho U^2} \right)^{-\mu/2} \left( \frac{\rho}{\delta} \right)^{(1-3\nu)/3} \quad (\text{strength}). \quad (1)$$

where  $H_2$  is a scaling constant. For large craters or weak materials, where crater growth is controlled principally by the target gravity, crater radius is instead independent of  $\pi_3$  and the scaling relationship takes the alternative form:

$$R \left( \frac{\rho}{m} \right)^{1/3} = H_1 \left( \frac{ga}{U^2} \right)^{-\frac{\mu}{2+\mu}} \left( \frac{\rho}{\delta} \right)^{\frac{2+\mu-6\nu}{3(2+\mu)}} \quad (\text{gravity}). \quad (2)$$

where  $H_1$  is a scaling constant.

Eqs. (1)–(2) apply to vertical impacts only. Previous numerical studies and laboratory experiments of oblique impacts suggest that crater volume and crater diameter decrease with decreasing impact angle, in a manner that is approximately consistent with the idea that only the vertical component of the impact velocity ( $U \sin(\theta)$ ) contributes to the growth of the crater in an oblique impact (Chapman and McKinnon, 1986; Elbeshhausen et al., 2009; Davison et al., 2011).

Using the same coupling parameter concept and point-source approximation, Housen and Holsapple (2011) developed a number of power-law scaling equations that relate properties of ejecta to the initial vertical impact conditions. In one such relationship, the speed of ejecta,  $v$ , is expressed as a function of ejecta launch position,  $r$ , as well as impactor and target properties (Housen et al., 1983; Housen and Holsapple, 2011):

$$\frac{v(r)}{U} = C_1 \left[ \frac{r}{a} \left( \frac{\rho}{\delta} \right)^\nu \right]^{-\frac{1}{\mu}} \left( 1 - \frac{r}{n_2 R} \right)^p, \quad (3)$$

where  $C_1$  and  $p$  are material dependant fitting constants. The relationship is also invalid for very fast ejecta, where  $r < n_1 a$  and  $n_1 \approx 1.2$ . To extend the relationship closer to the

impact point, [Raducan et al. \(2019\)](#) proposed an additional empirical term,  $\left(1 - \frac{r}{n_1 a}\right)^q$ , that includes the fast ejecta behaviour:

$$\frac{v(r)}{U} = C_1 \left[ \frac{r}{a} \left( \frac{\rho}{\delta} \right)^\nu \right]^{-\frac{1}{\mu}} \left( 1 - \frac{r}{n_2 R} \right)^p \left( 1 - \frac{r}{n_1 a} \right)^q, \quad (4)$$

where  $q$  is a target and material dependent constant. [Raducan et al. \(2019\)](#) found that for spherical aluminium projectiles at moderate velocities ( $U \approx 7$  km/s), the constant  $q$  takes values close to 0.2. However, further studies are needed to determine the influence of target and projectile properties on  $q$ .

The ejection speed decreases as the launch distance  $r$  increases. [Housen and Holsapple \(2011\)](#) defined the mass ejected at speeds larger than  $v$ ,  $M(> v)$ , as the mass of material  $M(< r)$  launched at distances from within  $r$ :

$$\frac{M(< r)}{m} = \frac{3k}{4\pi} \frac{\rho}{\delta} \left[ \left( \frac{r}{a} \right)^3 - n_1^3 \right]. \quad (5)$$

where  $k$  is a material fitting constant.

As with crater size scaling, no definitive extension to these ejecta scaling relationships exists for oblique impacts. Here we present some preliminary steps towards such an extension, based on our oblique impact simulation results.

### 3 Numerical model

To model the DART impact into possible asteroid surfaces we used the iSALE shock physics code ([Wünnemann et al., 2006](#)) in two and three dimensions. The iSALE shock physics code is a multi-material, multi-rheology extension of the SALE (Simplified Arbitrary Lagrangian Eulerian) hydrocode ([Amsden et al., 1980](#)) that was specifically designed for simulating impact processes and is similar to the older SALEB hydrocode ([Ivanov and Artemieva, 2002](#); [Ivanov et al., 1997](#)). iSALE-3D ([Elbeshausen et al., 2009](#); [Elbeshausen and Wünnemann,](#)

2011) uses a 3D solution algorithm very similar to the SALE-2D solver, as described by Hirt et al. (1974). The development history of iSALE-3D is described in Elbeshausen et al. (2009). Both codes share the same material modelling routines, including strength models suitable for impacts into geologic targets (Collins et al., 2004) and a porosity compaction model (Wünnemann et al., 2006). The crater sizes produced by iSALE-3D simulations of oblique impacts into aluminium targets agree well with laboratory experiments (Davison et al., 2011), while the ejection velocities and angles of ejecta produced by vertical impacts are in good agreement with data from laboratory impacts into sand (Luther et al., 2018; Raducan et al., 2019).

Here we aim to quantify the effect of impact angle on impact momentum transfer and ejecta mass and velocity distributions. Since full 3D simulations are very computationally expensive we performed a relatively small number of oblique impact simulations into targets with constant properties, for which we varied the impact angle. To get additional insight into the effects of key material properties on ejection angles we also revisited the Raducan et al. (2019) 2D simulations results. Raducan et al. (2019) studied the effects of material properties (cohesion, porosity and coefficient of internal friction) on ejection velocity and ejected mass in analog DART impacts. Here we re-analyse these results to quantify the dependence of ejection angle as a function of radius on target properties.

All the numerical simulations presented here used a  $\approx 620$  kg spherical aluminium projectile, impacting a porous, basaltic regolith target at 7 km/s. As in Raducan et al. (2019), the impactor was modelled using the Tillotson equation of state for aluminium (Tillotson, 1962) and a simple von Mises strength model.

Table 1: Material model parameters for impact simulations into Dimorphos analogues. For all simulated materials we used the thermal parameters from [Ivanov et al. \(2010\)](#).

Description	Impactor	iSALE-2D target	iSALE-3D target
Material	Aluminium	Basalt	Basalt
Impact angle ( $^\circ$ )	–	90	90/60/45/30
Impact speed (km/s)	–	7	7
Equation of state	Tillotson <sup>a</sup>	Tillotson <sup>b</sup>	Tillotson <sup>b</sup>
Strength model	von Mises	LUND <sup>c,d</sup>	LUND <sup>c,d</sup>
Poisson ratio <sup>c</sup> , $\nu$	0.33	0.25	0.25
Thermal parameters			
Melting temperature, $T_m$ (K)	933	1360	1360
$T_{frac}$	1.2	0.7	0.7
$A_{simon}$ (GPa)	6.0	4.5	4.5
$C_{simon}$	5.00	2.11	2.11
LUND strength parameters <sup>c,d</sup>			
Damage strength at zero pressure, $Y_0$ (kPa)	–	10	10
Strength at infinite pressure, $Y_{inf}$ (GPa)	–	1	1
Internal friction coefficient (damaged), $f$	–	0.2–1.2	0.6
Porosity model parameters ( $\epsilon - \alpha$ ) <sup>e</sup>			
Initial porosity, $\phi_0$	60%	10–50%	20%
Initial distension, $\alpha_0$	2.7	1.1–2.0	1.67
Distension at transition to power-law, $\alpha_x$	1.00	1.00	1.00
Elastic volumetric strain threshold, $\epsilon_{e0}$	0.00	$-1.88 \times 10^{-6}$	$-1.88 \times 10^{-6}$
Exponential compaction rate, $\kappa$	0.9	0.88–0.98	0.90

<sup>a</sup>Tillotson (1962); <sup>b</sup>Benz and Asphaug (1999); <sup>c</sup>Lundborg (1967); <sup>d</sup>Collins et al. (2004);

<sup>e</sup>Wünnemann et al. (2006).

The porous basaltic target model used here is considered to be a good approximation of the compositional structure of most asteroids. It comprises a Tillotson equation of state for basalt ([Tillotson, 1962](#); [Benz and Asphaug, 1999](#)) to describe the volumetric response of the solid of the target. The porosity compaction behaviour of the target material was described using the  $\epsilon - \alpha$  model ([Wünnemann et al., 2006](#); [Collins et al., 2011](#)). The  $\epsilon - \alpha$  input parameters were chosen so that the target crush-curve is consistent with shock wave and Hugoniot data for regolith-like materials ([Ahrens and Cole, 1974](#); [Raducan et al., 2020](#)). The target’s shear strength was modelled using a simple pressure-dependent strength model typical of geologic materials ([Lundborg, 1967](#); [Collins et al., 2004](#)), with a damaged strength at zero pressure,  $Y_0 = 10$  kPa. The impactor and target material properties are summarised in Table 1 and have been described in detail in [Raducan et al. \(2019\)](#).

To record the impact ejecta we followed the same approach as in [Raducan et al. \(2019\)](#): Lagrangian tracer particles were placed across the high-resolution domain and their mass,



velocity vector and launch position were then recorded at a fixed altitude, which was set to one impactor diameter. In the 3D simulations, launch position and azimuth were measured relative to the impact point.

### 3.1 iSALE-2D vs iSALE-3D

To verify consistency between iSALE-2D and iSALE-3D for predictions of ejected mass and momentum (i.e., that the results are independent of model geometry) we used both codes to simulate the same vertical impact scenario. The scenario considered was a DART impact into a homogeneous half-space, with the cohesive strength of the damaged material,  $Y_0 = 10$  kPa, coefficient of internal friction,  $f = 0.6$ , and initial porosity,  $\phi_0 = 20\%$ .

Figure 1 shows the mass-velocity-launch position ejecta distributions from three numerical simulations: two iSALE-2D runs and one iSALE-3D run. The three-dimensional (3D) simulation was limited to a spatial resolution of 5 cpr (3D, 5 cpr). For direct comparison, a 2D simulation of the same spatial resolution was performed (2D, 5 cpr). To assess the sensitivity of the results to the low spatial resolution of the 3D simulation, we also performed a 2D simulation that began with a resolution of 40 cpr and was subsequently coarsened using regridding to expedite the calculation without significant loss of accuracy (2D, regrid) as adopted in previous work (Raducan et al., 2019; Raducan et al., 2020) and the other 2D simulations presented here. Based on previous resolution studies (Raducan et al., 2019), the lower spatial resolution used in the 3D simulations is expected to under predict the crater volume by about 5% and the ejected momentum by about 10% compared to the 2D simulations with regridding.

Comparison between the 3D and 2D simulations with the same resolution (5 cpr) demonstrates consistency between iSALE-2D and iSALE-3D results (Fig. 1). In particular, the cumulative ejecta mass-velocity distributions and the cumulative ejected momentum-velocity distributions are nearly identical for the full range of ejection velocities. When compared to the results of the high-resolution 2D simulation where regridding was used (2D, regrid),

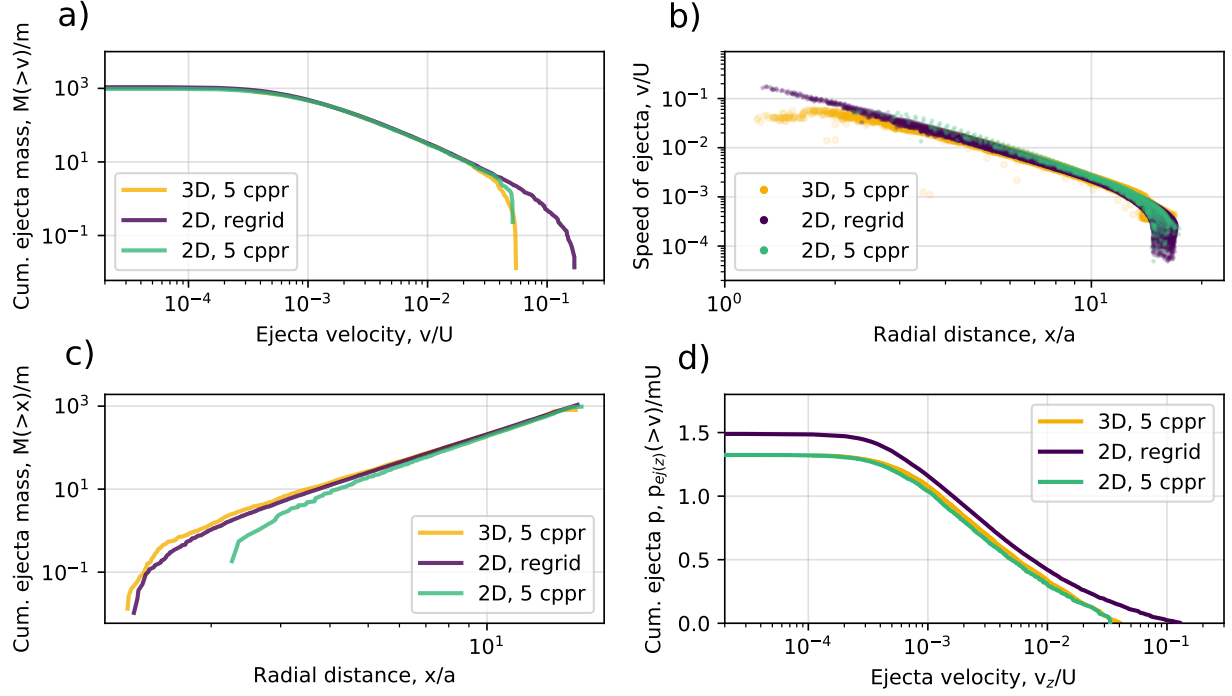


Figure 1: Mass-velocity-launch position distribution of ejecta from iSALE-2D simulations at 40 cppr and 5 cppr, compared with ejecta distribution from iSALE-3D at 5 cppr.

on the other hand, the 3D simulation results show good agreement in the cumulative mass and launch position of the slow ejecta, but fail to capture the fastest ejecta—known to require high spatial resolution at early times (Johnson et al., 2014). These fast particles, although of low mass, add  $\approx 10\%$  to the normalised cumulative ejected momentum in this example (Fig. 1d). As a result, the 3D simulation results presented here will systematically under-predict the cumulative ejected momentum.

## 4 Results

### 4.1 Influence of impact angle on net momentum transfer

Having verified the consistency between iSALE-2D and iSALE-3D simulation results for a vertical impact, we then used iSALE-3D to investigate the effect of impact angle on ejecta mass, velocity and angle distributions.

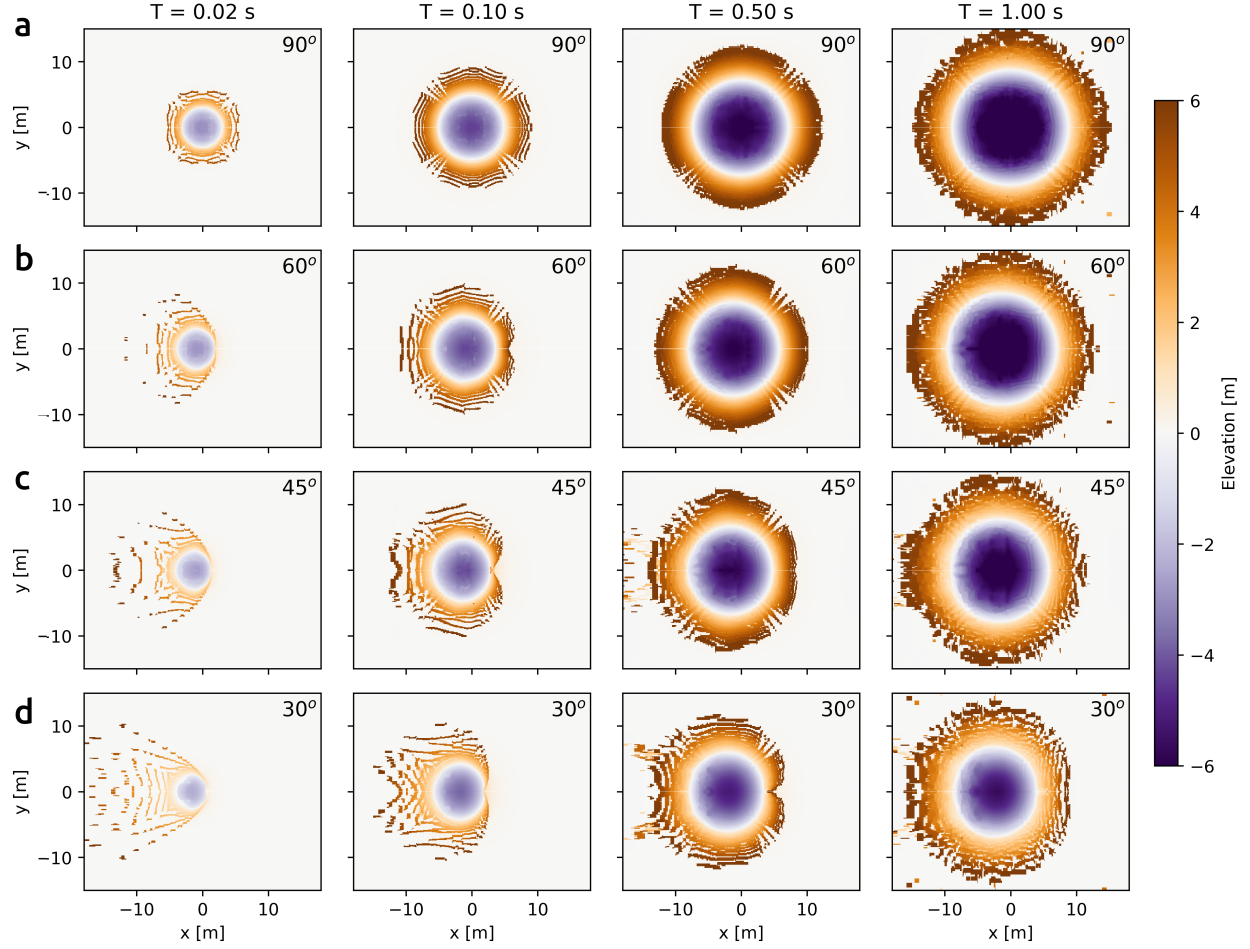


Figure 2: Surface topography of the DART impact at (a)  $90^\circ$ , (b)  $60^\circ$ , (c)  $45^\circ$  and (d)  $30^\circ$  degrees angles, captured at four different times: 0.02 s, 0.10 s, 0.40 s and 1.00 s. The impact direction is right to left.

Figure 2 shows the plan view of crater and ejecta curtain evolution following a DART impact at  $90^\circ$  (vertical),  $60^\circ$ ,  $45^\circ$  and  $30^\circ$  angles of incidence to the target surface. The impact speed is the same in all simulations ( $U = 7$  km/s); all other impactor and target properties are the same. The views are centered on the impact point (impactor tangent to the surface), with impact direction from right to left. The time frames of the oblique impacts (Figure 2b, c, d) show a highly asymmetric ejecta distribution at early times of the cratering process  $< 0.10$  s, compared to the same times in the vertical impact (Figure 2a). The asymmetric ejecta curtain becomes more symmetric as the crater grows towards its final size.

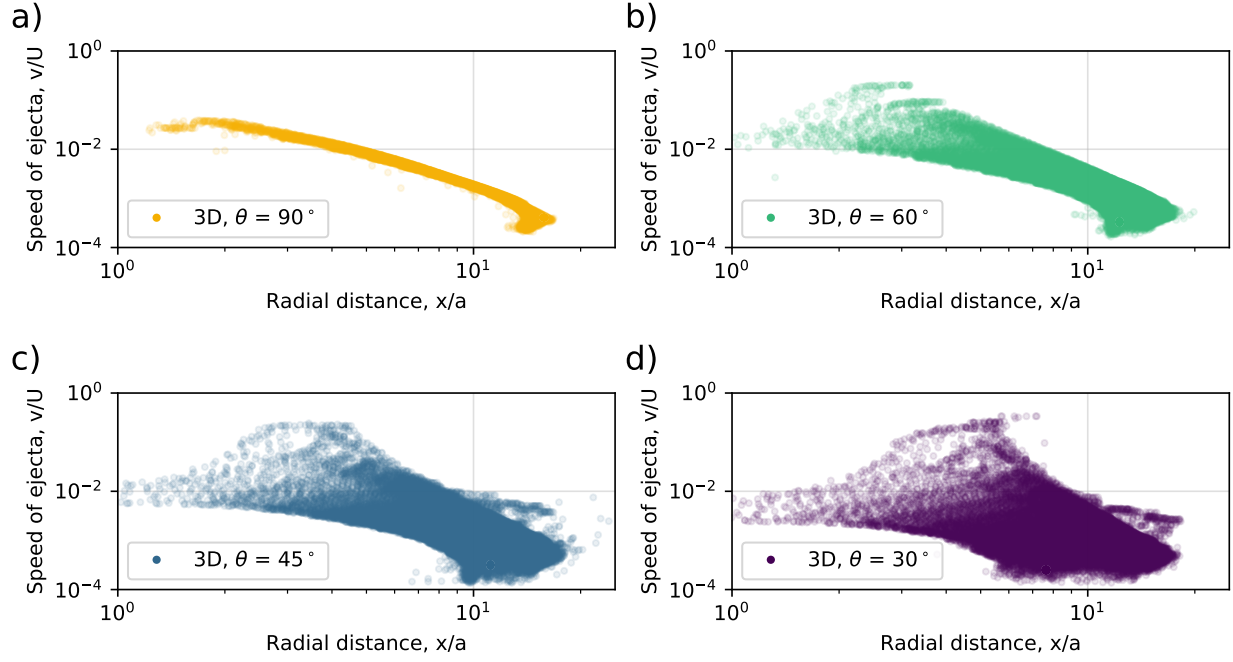


Figure 3: Velocity launch position distribution of the ejecta from impacts at 90, 60, 45 and 30 degrees angle of incidence.

The asymmetry in the ejecta is also illustrated by the velocity-launch position distribution of the ejected particles from the oblique impacts at 60, 45 and 30 degrees angle of incidence (Fig. 3). In all cases, the launch speed of the ejecta,  $v$ , was normalised by the impact speed,  $U$ , and plotted as a function of launch position,  $r$  (relative to the impact point), normalised by the impactor radius,  $a$ . The ejecta from the oblique impacts displays higher speeds in the downrange direction, and lower speeds in the uprange direction. This is consistent with previous laboratory-scale oblique impact experiments (Schultz, 1999; Anderson et al., 2003) and DART impact models (Stickle et al., 2015).

Following a similar approach to Anderson et al. (2004) to better understand how the ejecta velocity and ejection angle vary with azimuth around the impact point, we split the ejecta velocity distribution into azimuthal sections, between between  $\zeta = 0^\circ$ , which represents the uprange direction ( $-x$ ) and  $\zeta = 180^\circ$ , which represents the downrange direction ( $+x$ ). Figure 4 shows the surface topography of the DART impact at  $45^\circ$  impact angle and a diagram of the locations of the impact point, symmetry axis and the azimuth angles.

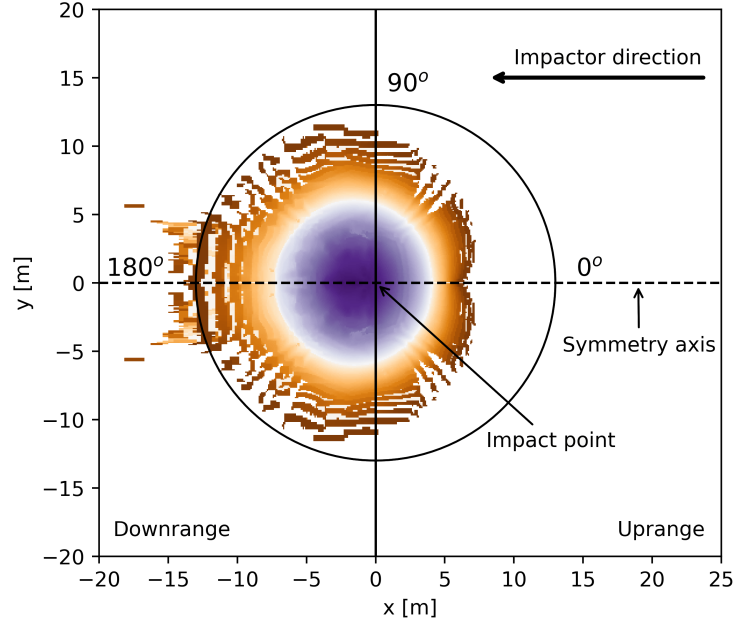


Figure 4: Surface topography of the DART impact at  $45^\circ$  angle of incidence, showing the direction of the impactor and the azimuthal ( $\zeta$ ) coordinates relative to the impact point.

Unlike in the vertical impacts, in oblique impacts the centre of the crater is not stationary, but instead moves from the impact point towards the downrange direction as the crater grows. When determining the normalised radial launch position of the ejecta,  $r/a$ , the origin was defined as the impact point, rather than the centre of the final crater. When the data from all azimuths is aggregated, this convention causes a larger spread in launch distance for a given ejection velocity compared to the  $90^\circ$  impact, and must be accounted for in the ejecta analysis. It also implies that the outermost launch position, which defines the approximate edge of the crater, varies with azimuth, even if the crater has a circular planform.

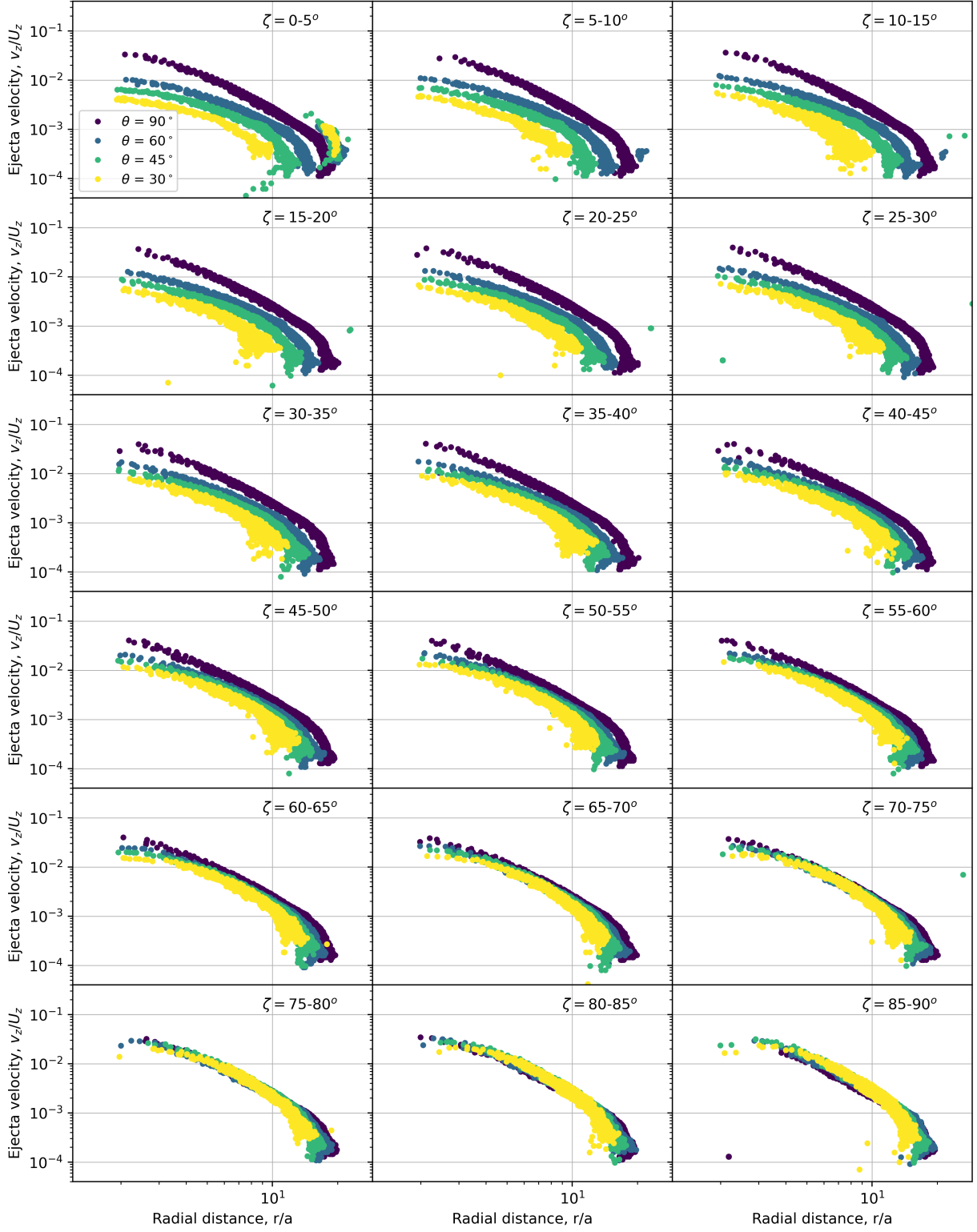


Figure 5: Ejecta vertical velocity - launch position distribution from vertical and oblique impacts ( $\theta = 90^\circ, 60^\circ, 45^\circ, 30^\circ$ ) at azimuth between  $\zeta = 0$  and  $\zeta = 90^\circ$ .

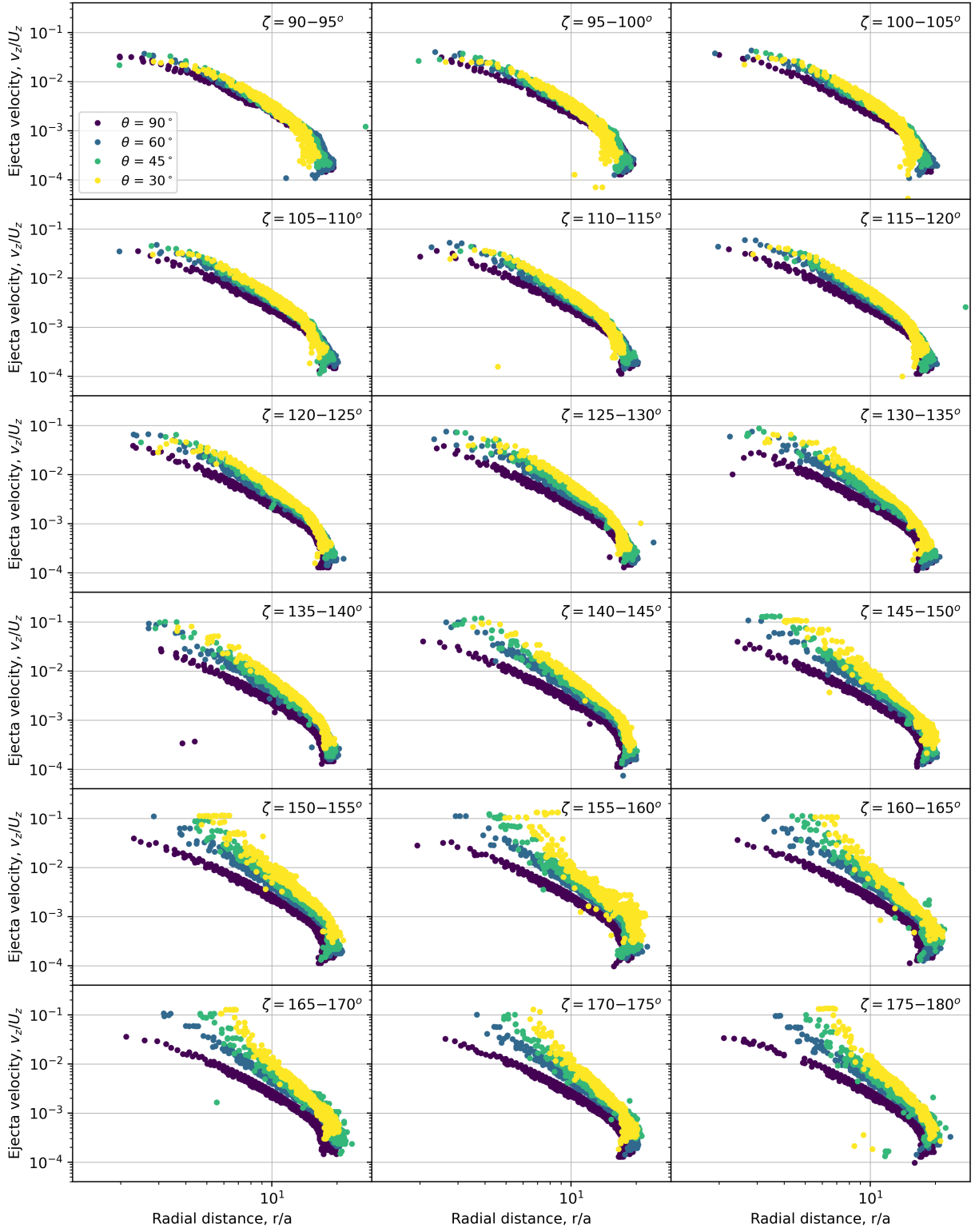


Figure 6: Ejecta vertical velocity - launch position distribution from vertical and oblique impacts ( $\theta = 90^\circ, 60^\circ, 45^\circ, 30^\circ$ ) at azimuth between  $\zeta = 90$  and  $\zeta = 180^\circ$ .

Figures 5 and 6 show the vertical component of the ejecta velocity normalised by the impact velocity,  $v_z/U_z$ , as a function of radial distance, normalised by the impactor size  $r/a$  and divided into  $5^\circ$  azimuthal segments, for four different impact angles. Here we analyse the vertical component of the ejection velocity as it is most relevant for momentum transfer. In the cross-range direction, at azimuths of about  $90^\circ$ , ejection velocity vs launch position is approximately independent of impact angle; however, ejection velocity vs launch position differs systematically with impact angle as azimuth approaches  $0^\circ$  (uprange) or  $180^\circ$  (downrange). In all cases, the middle part of the ejection velocity vs launch position trend is well approximated by a power-law.

Figures 7 and 8 show the ejection angle as a function of radial distance, normalised by the impactor size  $r/a$  and divided into  $5^\circ$  azimuthal segments, for four different impact angles. For azimuthal segments between  $\zeta = 0^\circ$  and  $\zeta = 90^\circ$ , the material is ejected at similar ejection angles, regardless of the impact angle (Fig. 7). However, between  $\zeta = 90^\circ$  and  $\zeta = 180^\circ$ , the ejection angle decreases with increasing azimuth. At the same time, impacts with lower impact angles,  $\theta$ , launch material out of the crater at lower ejection angles than in the vertical,  $\theta = 90^\circ$  case. For the four different impact angles, the ejection angle converges close to the crater rim.



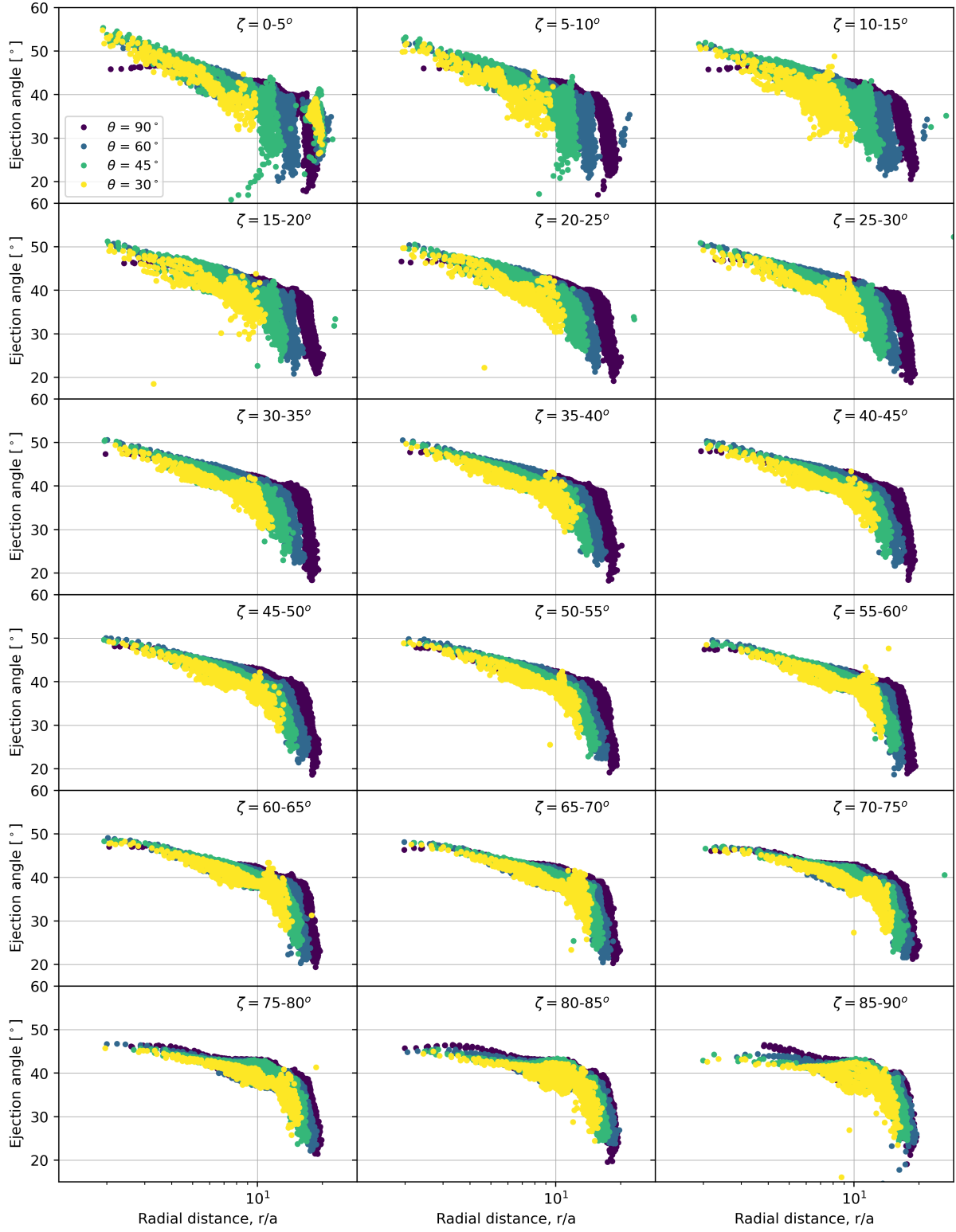


Figure 7: Ejection angle - launch position distribution from vertical and oblique impacts ( $\theta = 90^\circ, 60^\circ, 45^\circ, 30^\circ$ ) at azimuth between  $\zeta = 0$  and  $\zeta = 90^\circ$ .

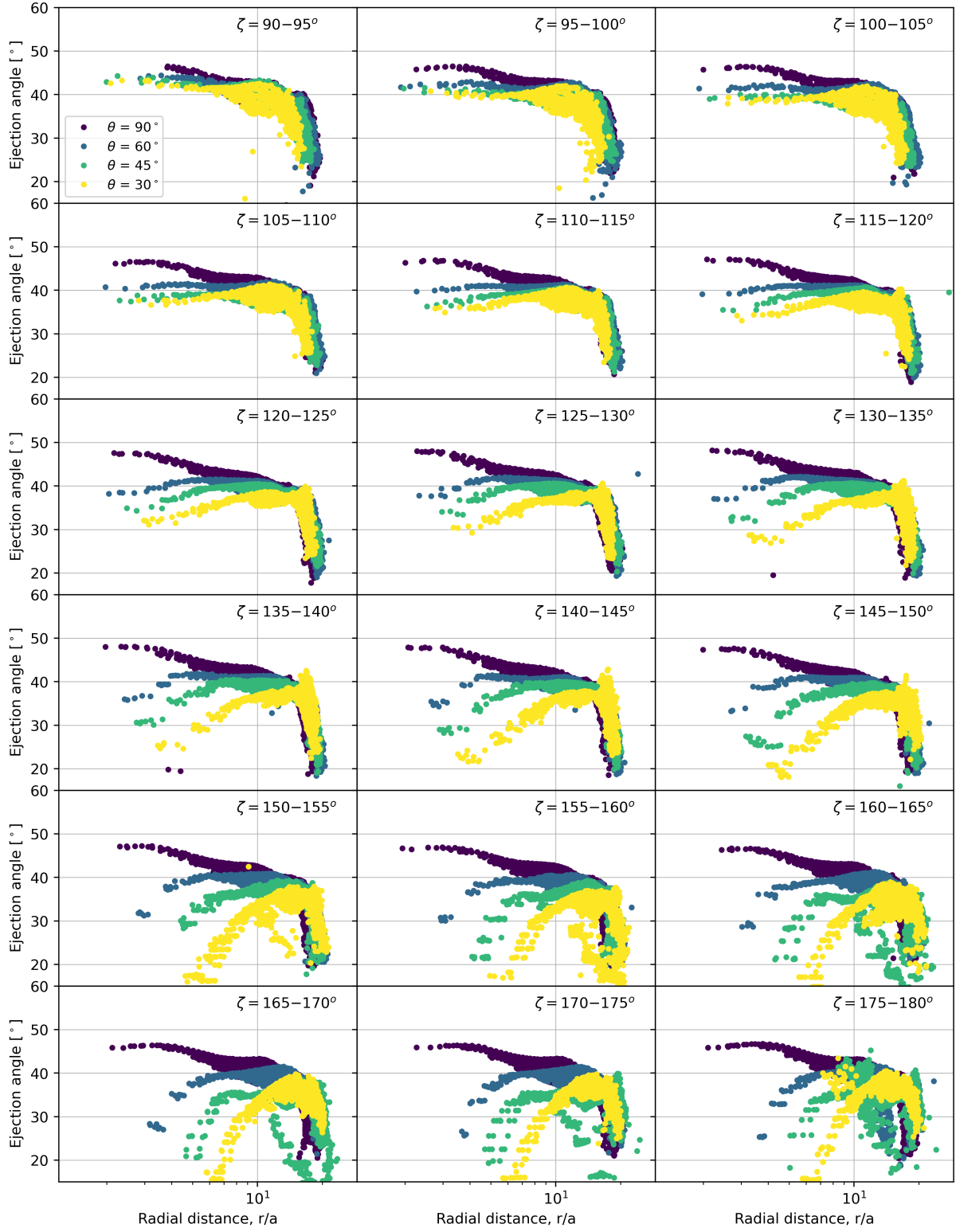


Figure 8: Ejection angle - launch position distribution from vertical and oblique impacts ( $\theta = 90^\circ, 60^\circ, 45^\circ, 30^\circ$ ) at azimuth between  $\zeta = 90$  and  $\zeta = 180^\circ$ .

The asymmetry of the ejecta can have important implications for momentum transfer. The net momentum of the target after the impact is the vector sum of the impactor momentum and the net ejected momentum vectors. Figure 9 shows the direction of the momentum vectors for the vertical ( $\theta = 90^\circ$ ) and oblique impacts ( $\theta = 60^\circ$ ,  $45^\circ$  and  $30^\circ$ ). The projectile imparts an initial momentum along the impact direction,  $\mathbf{P}_i = m\mathbf{U}$ , where  $m$  is the projectile mass and  $\mathbf{U}$  is the impact velocity vector. As most of the ejecta momentum is carried away in the downrange direction, the momentum imparted to the target by this ejecta,  $\mathbf{P}_{ej}$ , is mostly in the uprange direction. We define  $\psi_m$  as the angle of the imparted ejecta momentum vector  $\mathbf{P}_{ej}$  relative to the vertical. The vector sum of the impactor momentum vector and the imparted ejecta momentum vector is the target momentum,  $\mathbf{P}_t = \mathbf{P}_i + \mathbf{P}_{ej}$ . In the three oblique impact scenarios simulated here, the direction of  $\mathbf{P}_t$ , here defined by the angle  $\psi_t$ , is between the vertical and the downrange direction.

Figure 10 shows the direction of the momentum imparted by the ejecta,  $\psi_m$ , (Fig. 10a) and the direction of the total momentum,  $\psi_t$  (Fig. 10b), as a function of time, for the different impact angles.

As the crater grows towards its final diameter, the uprange direction of the ejecta momentum becomes more perpendicular to the surface. The direction of the net momentum imparted on the target also changes, from the downrange direction, towards the vertical direction. In the scenarios simulated here, for impacts into a 10 kPa target, the direction of the net momentum vector at the end of the crater growth is  $\psi_m \approx -18^\circ$  for the  $60^\circ$  impact,  $\psi_m \approx -30^\circ$  for the  $45^\circ$  impact and  $\psi_m \approx -45^\circ$  for the  $30^\circ$  impact.

In the simulations presented here crater growth is halted by the target strength before the ejected momentum direction becomes vertical. However, it is expected that with increasing cratering efficiency (e.g., decreasing strength), the ejecta momentum will make a larger contribution towards the total momentum vector (e.g., the ejecta momentum magnitude will dominate over the impactor momentum magnitude). At the same time, as the cratering efficiency increases, impacts at the same impact angle will become increasingly symmetric

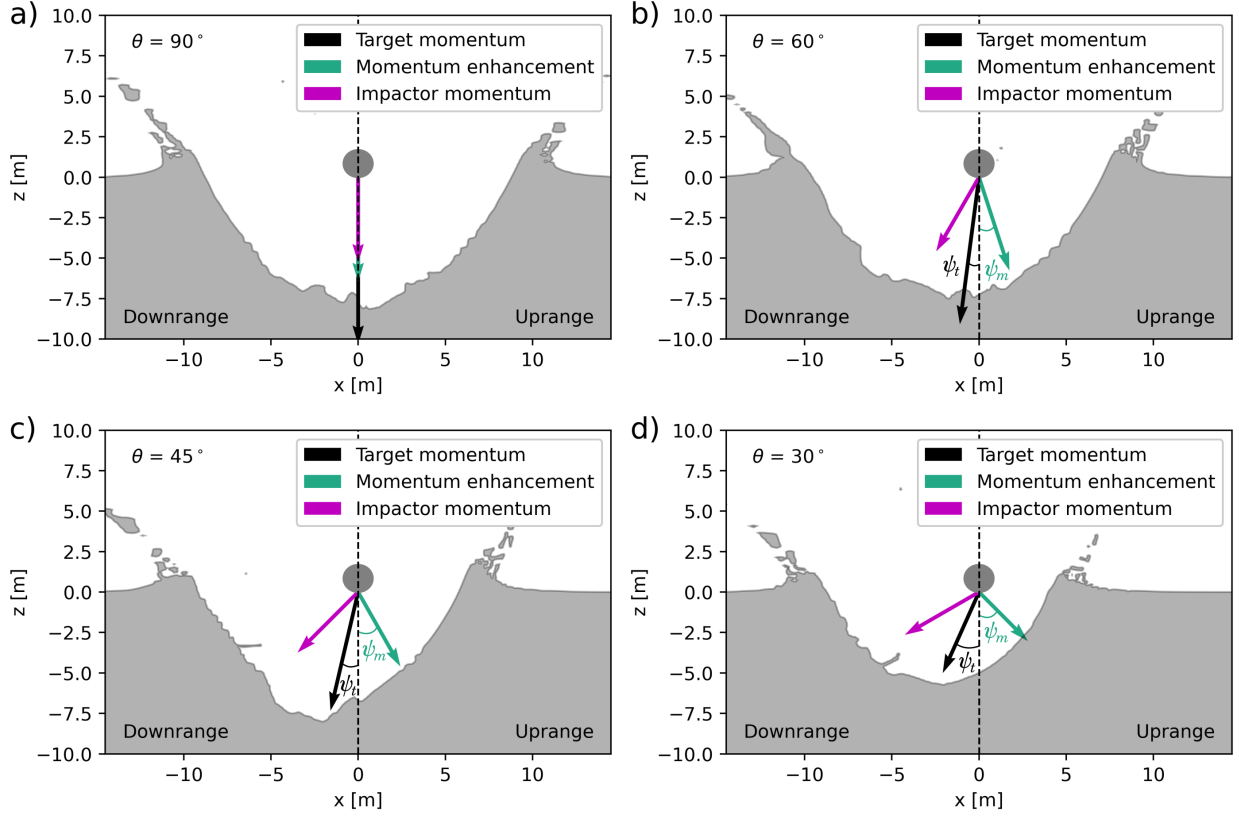


Figure 9: Crater profiles showing the direction of the momentum vectors at the end of crater growth. The impactor momentum is the momentum imparted directly from the impactor, the momentum enhancement is imparted by the ejected particles (makes an angle  $\psi_m$  relative to the vertical) and the target momentum is the net momentum of the target, after the impact (makes an angle  $\psi_t$  relative to the vertical). The impact direction is right to left.

and both the ejected and total momentum vectors will be closer to the vertical,  $\psi_t \approx \psi_m \approx 0^\circ$ . To test this, more numerical simulations of oblique impacts into targets with lower strength are needed, however due to the increased cratering efficiency, such simulations are very computationally expensive.

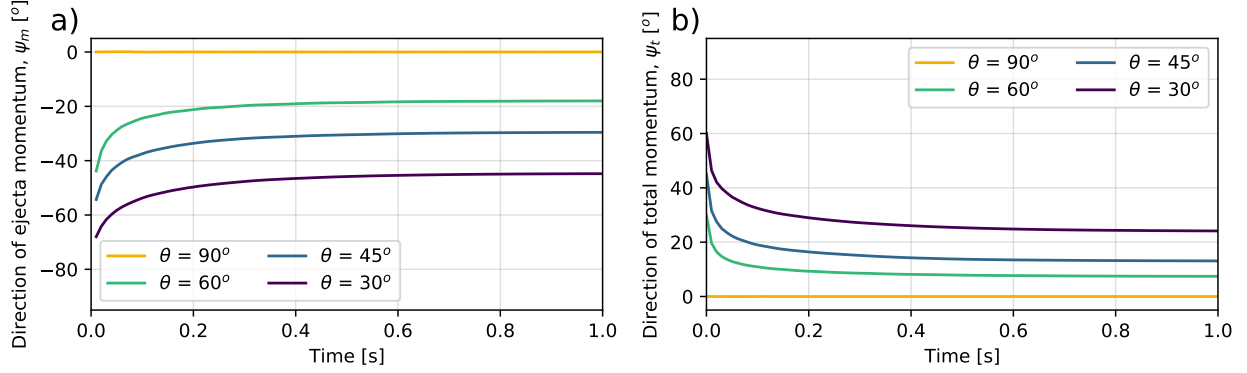


Figure 10: Direction of the (a) ejecta momentum and (b) total momentum from vertical,  $90^\circ$ , and oblique,  $60^\circ$ ,  $45^\circ$  and  $30^\circ$ , angle of incidence. The direction is measured anticlockwise from the negative  $x$ -axis (downrange,  $0^\circ$ ) to the positive  $x$ -axis (uprange,  $180^\circ$ ).

## 4.2 The effects of target properties on the ejection angle

Raducan et al. (2019) quantified the effects of target porosity and target coefficient of internal friction on the launch speed of crater ejecta in vertical impacts but the corresponding ejection angles were not reported. Here we present ejection angle results from the same suite of simulations to provide context for our 3D simulation results and to inform analytical approximations of ejecta plume evolution.

Figures 11(a) and (c) show ejection velocity, normalised by the impact velocity,  $v/U$ , and ejection angle, respectively, as a function of normalised radial distance from the impact point,  $r/a$ , for vertical impacts into targets with fixed cohesion,  $Y_0 = 10$  kPa, and fixed coefficient of internal friction,  $f = 0.6$ . For these targets the initial porosity,  $\phi_0$ , was varied between 10% and 50%. Increasing the target porosity has the effect of reducing the launch speed and ejection angle of the material ejected close to the impact point.

Figures 11(b) and (d) show normalised ejection velocity and ejection angle as a function of normalised radial distance for impacts into 10 kPa, 20% porous targets, for which the coefficient of internal friction,  $f$ , was varied between 0.2 and 1.2. Increasing the target coefficient of internal friction has the effect of reducing the launch speed of the material ejected close to the crater rim and the ejection angle. The ejecta velocity-launch position

distribution from both parameter studies is discussed in more detail in (Raducan et al., 2019).

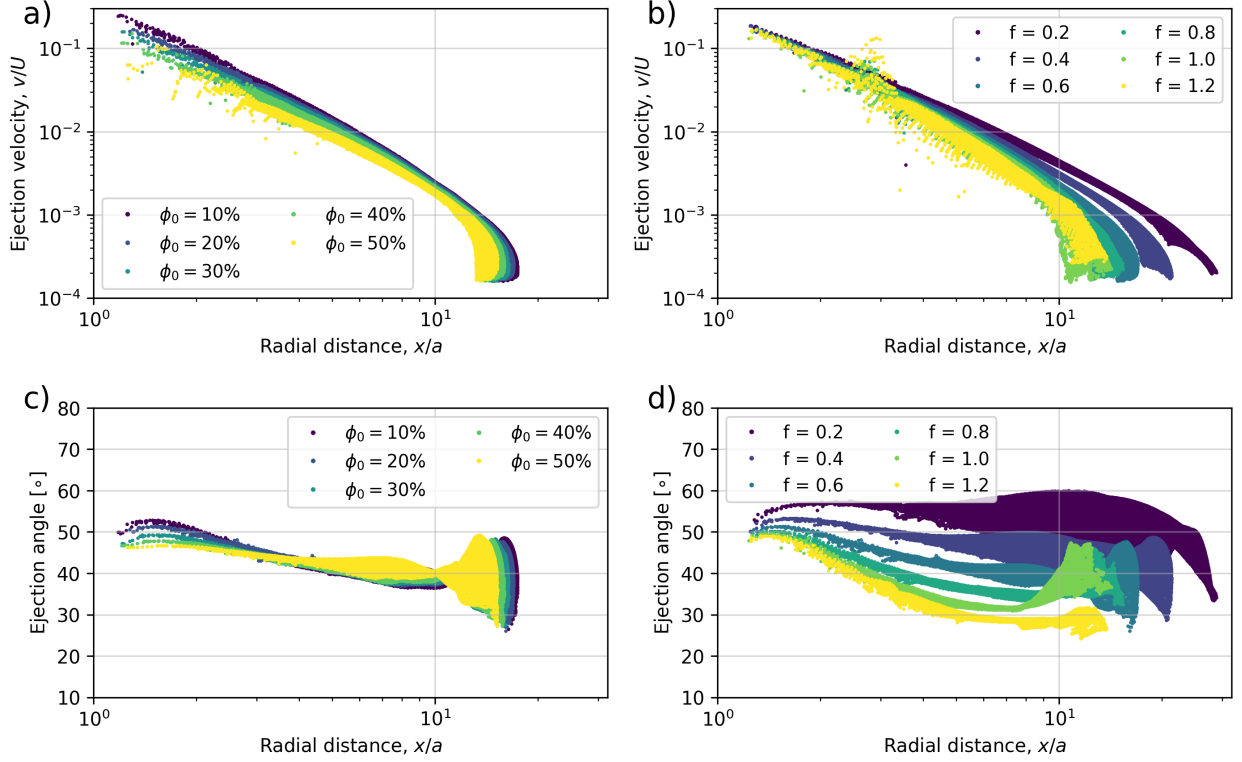


Figure 11: (a, b) Velocity – launch position distribution of ejecta from impacts into a 10 kPa target, with varying porosity,  $\phi_0$  and varying coefficient of friction,  $f$ . a) represents the ejecta velocity distribution for impacts with  $Y_0 = 10$  kPa,  $f = 0.6$  and  $\phi_0$  between 10 and 50%. b) represents the ejecta velocity distribution for impacts with  $Y_0 = 10$  kPa,  $\phi_0 = 20\%$  and  $f$  between 0.2 and 1.2. (c, d) Ejection angle – launch position distribution of ejecta from impacts into a 10 kPa target, with varying  $\phi_0$  (c) and varying  $f$  (d).

It is often assumed that the ejection angle of individual ejecta particles is approximately  $45^\circ$  to the target surface, independent of launch position. However this assumption does not always hold and the mean ejection angle can vary significantly with time and launch distance, depending on the physical characteristics of the target material, such as porosity or internal friction coefficient (Hoerth et al., 2013; Gulde et al., 2018; Luther et al., 2018).

Figure 11(c) shows that fast ejecta is launched at steeper ejection angles when target porosity is lower. However, the ejection angle converges at radial distances larger than  $4a$  such that the ejection angle of slower ejecta is relatively insensitive to target porosity.

Figure 11(d) shows that ejection angle decreases with launch position, by up to  $20^\circ$ . At the same time, the average ejection angle decreases with increasing coefficient of internal friction, from about  $60^\circ$  for  $f = 0.2$ , to about  $30^\circ$  for  $f = 1.2$ . Similar trends have been observed for vertical impacts in the gravity regime (Luther et al., 2018).

## 5 Discussion

### 5.1 Towards an ejecta scaling relationship for oblique impacts

Ejecta scaling relationships are useful to determine the ejecta mass-velocity distribution and momentum transfer for vertical impacts scenarios other than the ones considered here. However, most planetary impacts are oblique and the existing scaling relationships (Housen and Holsapple, 2011) only apply to vertical impacts. Therefore, the current point-source scaling theory needs to be extended and adapted to oblique impacts.

Previous attempts at determining the ejecta distribution from oblique impacts empirically include the studies by Anderson et al. (2003), Anderson et al. (2004) and Richardson et al. (2007). Anderson et al. (2003) conducted impact experiments of  $\approx 6$  mm diameter aluminium spheres into medium-grained sand, at  $90^\circ$  and  $30^\circ$  impact angles and an impact velocity of 1 km/s. From each impact experiment they recorded the ejection velocities, angles, and positions of the ejecta expelled at one moment during the first half of the crater growth. They observed that in the oblique impact cases, the velocity distribution of the ejected particles varies with azimuth from the impact point relative to the trajectory direction. They defined the ratio between the downrange and the uprange ejection velocities (DR/UR) as a measure of the asymmetry in the ejecta curtain. At early times, they recorded a 40% increase in the ejection velocity from the uprange to the downrange sides of the crater. At later times, about when the crater radius reached about half of the final radius, the difference between the velocities in the uprange and in the downrange sides of the craters decreased to about 20%. Anderson et al. (2004) ran additional impact experiments at  $45^\circ$  impact angles

and tried to use the Maxwell Z-Model to predict the ejection velocities and ejection angles. One major difficulty with deriving a scaling law using this approach was the assumption that there is a single, stationary point source.

The work in this section attempts to develop an ejecta scaling relationship for oblique impacts, based on numerical simulation data. The three-dimensional simulations of the DART impact into a 10 kPa, 20% porous target, at vertical, 60°, 45° and 30° impact angles presented above are used here to provide information about the ejecta distribution as a function of impact angle.

Fitting Eq. (3) through the ejection velocity-launch position distributions shown in Figures 5 and 6 (where  $U$  is the vertical component of the impact velocity,  $U_z$ ), allows us to determine  $\mu$  and  $C_1$  for each azimuth and impact angle investigated. The azimuthal radius,  $R_\zeta$ , which here is defined as the distance between the impact point and the crater rim for each azimuthal segment can also be determined. Similarly, the constant  $k$  can be found by fitting Eq.(5) to the cumulative ejected mass-launch position data.

Figure 12 shows the best fit constants  $\mu$  (Fig. 12a),  $C_1$  (Fig. 12b),  $k$  (Fig. 12c) and  $R_\zeta$  (Fig. 12d) as a function of azimuth,  $\zeta$ , for the four different impact angles. The constants were normalised by the average  $\mu$ ,  $C_1$ ,  $k$  and  $R$  constants found for the  $\theta = 90^\circ$  impact scenario. All four constants,  $\mu$ ,  $C_1$ ,  $k$  and  $R_\zeta$ , vary as periodic functions of impact angle and azimuth around the impact point. In this work, simple trigonometric functions are fit through these distributions as a function of azimuth for each impact angle.

The coupling parameter velocity exponent,  $\mu(\zeta, \theta)$ , can be approximated by

$$\mu(\zeta, \theta) \approx \mu \times \left[ 1 + \frac{1}{2} \cos(\zeta) \cos(\theta) \right], \quad (6)$$

where  $\mu$  is the velocity exponent in the vertical impact scenario. The constant  $C_1(\zeta, \theta)$  varies as an exponential of cosine

$$C_1(\zeta, \theta) \approx C_1 \times \exp[-5 \cos(\zeta) \cos(\theta)], \quad (7)$$



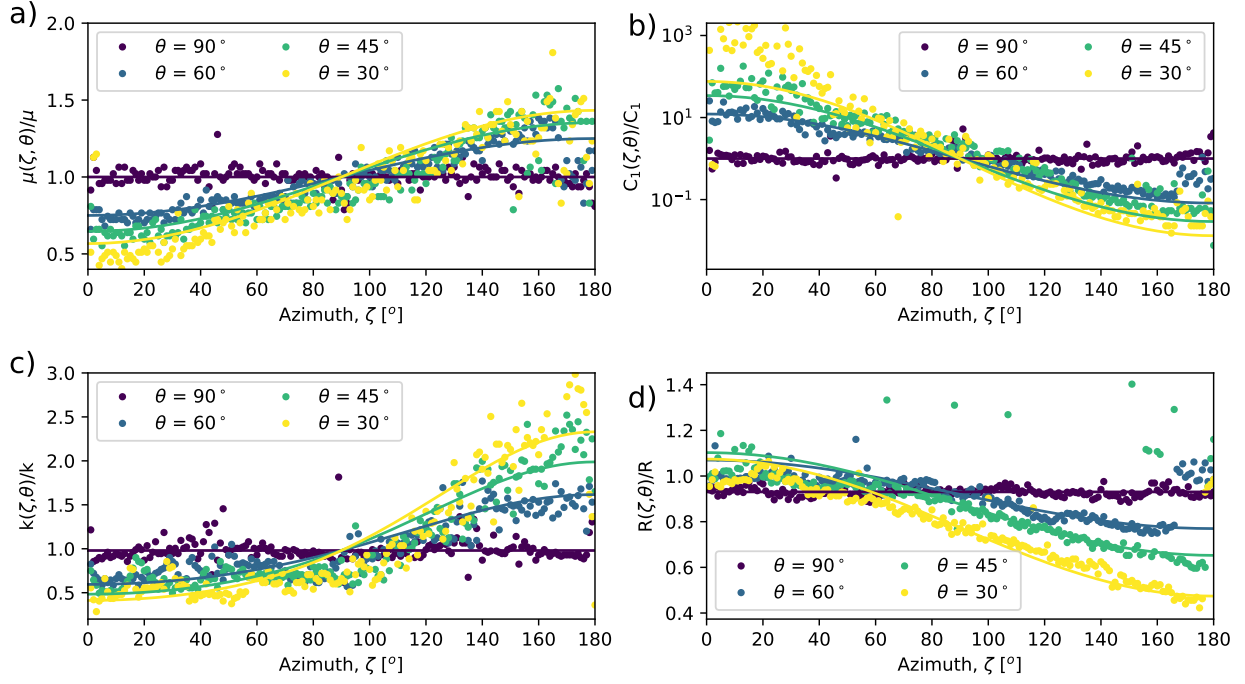


Figure 12: Constants (a)  $\mu$ , (b)  $C_1$ , (c)  $k$  and (d)  $R$ , normalised by the average value in the  $90^\circ$  impact scenario, as a function of azimuth around the crater (centred at the impact point).

where  $C_1$  is the constant derived for the vertical impact scenario.

$$k(\zeta, \theta) \approx \frac{k}{n_\zeta} \times \exp[-0.02 \cos(\zeta) \cos(\theta)], \quad (8)$$

where  $k$  is the constant derived for the vertical impact scenario and  $n_\zeta$  is the number of azimuthal segments considered.

$$R(\zeta, \theta) \approx R \times \left[ 1 - \frac{(90 - \theta)}{100} \times \frac{\cos(\zeta)}{2} \right], \quad (9)$$

where  $R$  is the crater radius in the vertical impact scenario. These trigonometric functions were plotted in Figure 12.

## 5.2 Comparison of the oblique impact ejecta scaling relationship with laboratory experiments

Equations (6)–(9), can be used together with Eqs. (3)–(5) to determine the ejection velocity as a function of launch position and azimuth for an oblique impact, given known scaling constants ( $\mu$ ,  $C_1$ ,  $k$ ,  $R$ ). Here we present a methodology for using these equations to approximate the distribution of ejection velocities from an oblique impact, at fixed times during crater growth, using only information that can be derived from an equivalent vertical impact. To test our methodology, we used the experimental ejection velocity data recorded at several different radial distances from the impact point for laboratory-scale impacts into sand at a speed of  $\approx 1$  km/s and at impact angles of both  $30^\circ$  and  $90^\circ$  to the horizontal (Anderson et al., 2003).

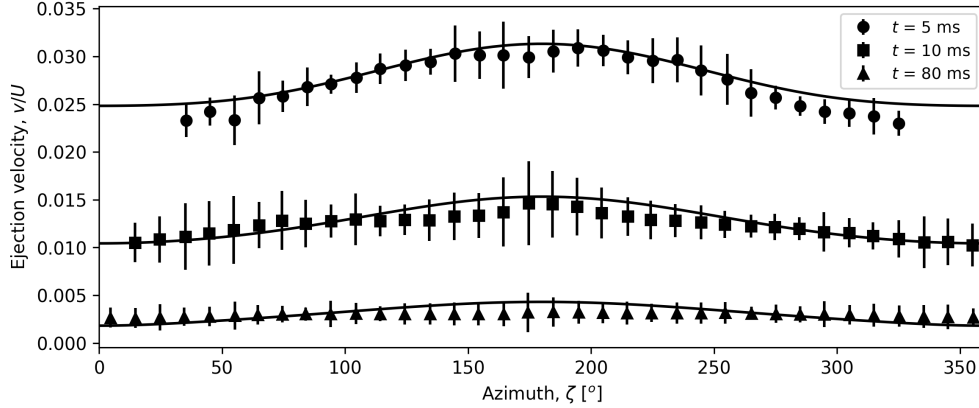


Figure 13: Average ejection velocity from  $\approx 1$  km/s oblique  $30^\circ$  impacts into sand conducted in laboratory by (Anderson et al., 2003), as a function of azimuth around the crater, at three different times:  $t = 5$ , 10 and 80 ms. The error bars were calculated as  $1\sigma$  (Richardson et al., 2007). Our semi-analytical approximation of the ejection velocity from Eqs. (6)–(7) and Eq. (4) was plotted for comparison.

The first step is to derive the scaling constants  $\mu$  and  $C_1$  from ejection velocity data for a vertical impact into the same target material and otherwise similar impactor parameters to the oblique impacts in question. The vertical impact experiments of Anderson et al. (2003) are presented in the form of  $v/(gR)^{1/2}$  versus  $x/R$ , where  $v$  is ejection speed,  $R$  is the

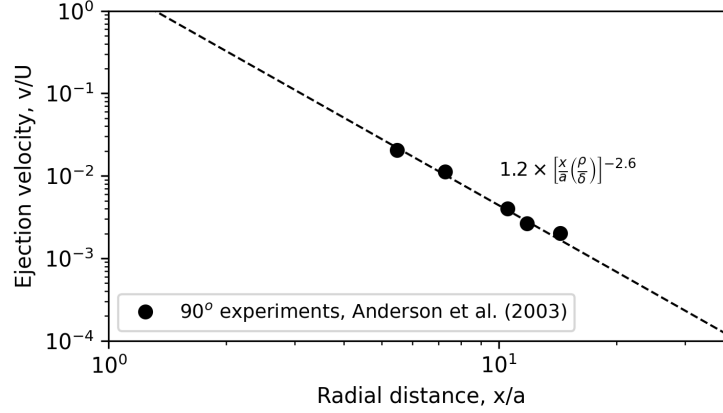


Figure 14: Ejection velocity vs radial distance distribution of ejecta from  $\approx 1$  km/s vertical impacts (Anderson et al., 2003).

apparent crater radius and  $x$  is the launch position. Ejection velocity and radial distance were therefore converted into  $v/U$  and  $x/a$  values using an apparent crater radius of  $R = 8.1$  cm (see Housen and Holsapple (2011) for details), where  $a = 3.175$  mm (Fig. 14). By fitting Eq. (3) to the rescaled experimental data, we derived  $\mu = 0.38$ ,  $C_1 = 1.23$ .

The next step is to substitute these derived constants into Eqs. (6)–(7), which can then be substituted into Eq. (4). Here we used  $\nu = 0.4$ ,  $n_1 = 1$ ,  $n_2 = 1.2$ ,  $p = 0.3$ , as derived by Housen and Holsapple (2011) for impacts into sand, and  $q = 0.2$  (Raducan et al., 2019). In these experiments, the crater radius was measured as  $R = 8.1$  cm (Housen and Holsapple, 2011), however the crater radius can also be approximated from Eq. (1) (or Eq. (2) for the strength regime).

Figure 13 shows the average ejection velocity as a function of azimuth, as measured by Anderson et al. (2003), at 5, 10 and 80 ms after impact. For comparison, our analytical approximation of the ejection velocity (Eq. (4)) from a  $30^\circ$  impact as a function of azimuth,  $\zeta$ , is plotted as a continuous line. To convert from radial launch position to ejection time, we follow the approach of Richardson et al. (2007): at 5 ms,  $x/a \approx 0.2$ ; at 30 ms,  $x/a \approx 0.3$ ; at 80 ms,  $x/a \approx 0.5$ .

Our semi-analytical model of ejection velocities shows a generally good agreement with the experimental data. The match is least impressive at late times, close to the crater

rim. The laboratory experiments presented here have a much higher cratering efficiency than the numerical simulations used to derive the trigonometric functions used here, which might be the source of the discrepancy. Therefore, for cratering events with much larger cratering efficiencies than our simulations one should apply caution when using our approach to approximate the velocity distribution of the slow ejecta from oblique impacts.

### 5.3 Semi-analytical approximation for the momentum enhancement from oblique impacts

The efficiency of impact momentum transfer is often expressed in terms of a factor  $\beta$ , which for a vertical impact is simply the ratio of the momentum transferred to the target  $M\Delta v$  (where  $M$  is the target mass and  $\Delta v$  is the velocity change) divided by the impactor momentum  $mU$ . More generally, the conservation of momentum can be defined as:

$$M\Delta\mathbf{v} = m\mathbf{U} + m(\beta - 1)(\hat{\mathbf{n}} \cdot \mathbf{U})\hat{\mathbf{n}} + m(\gamma - 1)(\hat{\mathbf{t}} \cdot \mathbf{U})\hat{\mathbf{t}} \quad (10)$$

where  $\hat{\mathbf{n}}$  and  $\hat{\mathbf{t}}$  are the inward surface normal, and downrange directed surface tangent unit vectors, respectively. In our simulations of impacts into a flat target, with the impact trajectory in the  $x$ - $z$  plane, the inward surface normal vector is in the negative vertical direction  $-z$  and the downrange surface tangent vector is  $-x$ . The first term on the right-hand side is the momentum imparted directly by the impactor  $\mathbf{P}_i$ ; the second term is the component of the momentum imparted by the escaping ejecta that acts normal to the surface; the third term is the component of the momentum imparted by the escaping ejecta that acts parallel to the surface, positive in the downrange direction. If the net momentum imparted to the target by the escaping ejecta can be assumed to act along the surface normal vector (i.e.,  $\psi_m = 0$ ) then the third term can be neglected (Feldhacker et al., 2017; Cheng et al., 2020). However, for the scenarios simulated here  $|\psi_m| > 0$  and so we retain the full expression.

According to Equation 10, the definition of  $\beta$  (and  $\gamma$ ) can be expressed in terms of the normal (and tangential) components of the momentum transfer and incident moment:

$$\beta = \frac{M\hat{\mathbf{n}} \cdot \Delta \mathbf{v}}{m\hat{\mathbf{n}} \cdot \mathbf{U}} = \frac{M\Delta v \cos \psi_t}{mU \sin \theta}, \quad (11)$$

$$\gamma = \frac{M\hat{\mathbf{t}} \cdot \Delta \mathbf{v}}{m\hat{\mathbf{t}} \cdot \mathbf{U}} = \frac{M\Delta v \sin \psi_t}{mU \cos \theta}. \quad (12)$$

Alternatively,  $\beta$  and  $\gamma$  can be expressed in terms of the normal and tangential components of the net ejecta momentum  $\mathbf{P}_{\text{ej}}$ :

$$\beta - 1 = \frac{\hat{\mathbf{n}} \cdot \mathbf{P}_{\text{ej}}}{m\hat{\mathbf{n}} \cdot \mathbf{U}} = \frac{P_{\text{ej}} \cos \psi_m}{mU \sin \theta}, \quad (13)$$

$$\gamma - 1 = \frac{\hat{\mathbf{t}} \cdot \mathbf{P}_{\text{ej}}}{m\hat{\mathbf{t}} \cdot \mathbf{U}} = \frac{P_{\text{ej}} \sin \psi_m}{mU \cos \theta}. \quad (14)$$

Hence,  $\beta$  and  $\gamma$  are related by:

$$(\gamma - 1) = (\beta - 1) \tan \theta \tan \psi_m \quad (15)$$

for  $\theta < 90$  and  $|\psi_m| < 90$ . Note that for vertical impacts  $\gamma = 0$  and  $(\gamma - 1) = 0$  if the net ejecta momentum is directed exactly normal to the target ( $\psi_m = 0$ ).

For a vertical impact ( $\theta = 90$ ,  $\psi_m = 0$ ), [Cheng et al. \(2016\)](#) showed that the vertical momentum carried away by the ejecta from a vertical impact,  $\beta - 1$ , can be found from integrating the differential mass,  $dM$  (from Eq. (5)), within the radial distance range from  $n_1$  to  $n_2 R/a$

$$P_{\text{ej}} = \frac{9km}{4\pi} \frac{\rho}{\delta} \int_{n_1}^{\frac{n_2 R}{a}} w^2 v_z dw, \quad (16)$$

where  $w = r/a$  and  $v_z$  is the vertical component of the ejection velocity. The vertical momentum carried away by the ejecta,  $\beta - 1$  is then:

$$\beta - 1 = \frac{P_{\text{ej}}}{mU} = \frac{9k}{4\pi} \frac{\rho}{\delta} \int_{n_1}^{\frac{n_2 R}{a}} w^2 \frac{v_z}{U} dw. \quad (17)$$

To generalise this approach for oblique impacts, we define the vertical ejecta momentum,  $\beta - 1$ , as the sum of the momentum calculated for each azimuth wedge:

$$\beta - 1 = \frac{\hat{\mathbf{n}} \cdot \mathbf{P}_{\text{ej}}}{m\hat{\mathbf{n}} \cdot \mathbf{U}} = \frac{P_{ej} \cos \psi_m}{mU \sin \theta} \approx 2 \times \sum_{i=1}^{n_\zeta} \frac{9k_\zeta \rho}{4\pi \delta} \int_{R_\zeta}^{n_1^a} \frac{v_z(w)}{U_z} w^2 dw \quad (18)$$

where  $w = r/a$ ,  $k_\zeta = k/n_\zeta$  and  $n_\zeta$  is the number of azimuthal wedges between  $\zeta = 0$  (uprange) and  $\zeta = 180$  (downrange). To evaluate the integral requires that we substitute the power-law approximation of Eq. (3) with parameters appropriate for each azimuthal wedge into Eq. (18), noting that the relevant normalised ejection velocity component is  $v_z/U_z$ . In this case, the momentum enhancement can be approximated by

$$\beta - 1 \approx 2 \times \sum_{i=1}^{n_\zeta} \frac{9k(\zeta_i, \theta) \rho}{4\pi \sin \theta \delta} \int_{n_1}^{\frac{n_2 R(\zeta_i, \theta)}{a}} \left[ C_1(\zeta_i, \theta) \left[ (w) \left( \frac{\rho}{\delta} \right)^\nu \right]^{-1/\mu(\zeta_i, \theta)} \right] w^2 dw. \quad (19)$$

To calculate  $\beta - 1$  for a given set of constants, Eq. (19) must be solved numerically.

Equation (19) provides a framework for estimating  $\beta - 1$  for an impact with known impactor ( $m$ ,  $U$ ,  $\delta$ ,  $\theta$ ) and target parameters ( $\rho$ ). It requires knowledge of the azimuthal and angle dependence of the ejecta distribution parameters  $k(\zeta, \theta)$ ,  $C_1(\zeta, \theta)$  and  $\mu(\zeta, \theta)$  as well as the azimuthal and angle dependence of the crater rim radius, relative to the impact point  $R(\zeta, \theta)$ . With knowledge of the ejecta imparted momentum vector angle to the vertical,  $\psi_m$ ,  $\gamma - 1$  can be determined from  $\beta - 1$  using Eq. 15.

Equations (6)-(9) approximate these relationships for impacts similar to those simulated here and may be more broadly applicable given the promising comparison with experimental data. However, the required values of these parameters can also be determined for each azimuth and impact angle from individual simulation results. To measure the error in each level of approximation, we compare the total integrated vertical ejected momentum for each impact angle, as determined by summing the contribution of each ejected tracer particle, with two estimates of the total ejected momentum. In Table 2 the total vertical momentum of the ejecta as derived from summing the contribution of each ejected tracer particle from

each simulation is defined as ‘Measured  $\beta - 1$ ’. The first estimate of the ejecta vertical momentum (‘Best-fit  $\beta - 1$ ’ in Table 2) comes from using Eq. (19) and individual analytical best-fit constants ( $\mu$ ,  $C_1$ ,  $k$  and  $R_\zeta$ ) for each azimuth as shown in Fig. 12. The second estimate (‘Analytical  $\beta - 1$ ’ in Table 2) was obtained from using Eq. (19) and the analytical expressions for:  $\mu(\zeta, \theta)$  (Eq. (6)),  $C_1(\zeta, \theta)$  (Eq. (7)),  $k(\zeta, \theta)$  (Eq. (8)) and  $R(\zeta, \theta)$  (Eq. (9)). Raducan et al. (2019) determined that for a vertical impact into a 1 kPa, 20% porous target the fitting constants are  $\mu \approx 0.42$ ,  $C_1 \approx 1.1$  and  $k \approx 0.4$ . Here we used Eq. (19) to find an analytical approximation of  $\beta - 1$  for this set of scaling constants. Our comparison between the three different measures of  $\beta - 1$  show that both estimates are within 2% of the ‘measured’  $\beta - 1$  for a  $90^\circ$  impact and within 20% for a  $30^\circ$  impact.

Table 2: Normal ejecta momentum,  $\beta - 1$ , and tangential ejecta momentum,  $\gamma - 1$ , measured from the Lagrangian tracers, compared with  $\beta - 1$  calculated from the best-fit constants and calculated using the newly derived analytical approximations (Eq. (19)).

	Impact angle			
	$90^\circ$	$60^\circ$	$45^\circ$	$30^\circ$
Measured $\beta - 1$	1.32	1.36	1.33	1.24
Direction ejecta momentum, $\psi_m$	$0.03^\circ$	$-18.00^\circ$	$-29.57^\circ$	$-44.79^\circ$
Direction total momentum, $\psi_t$	$0.02^\circ$	$7.42^\circ$	$13.09^\circ$	$24.13^\circ$
Measured $\gamma - 1$	0.00	-0.38	-0.53	-0.61
Best-fit $\beta - 1$	1.24	1.35	1.37	1.02
Analytical $\beta - 1$	1.30	1.35	1.36	1.52

For the impact scenarios studied here, the vertical efficiency of the momentum transfer seems to be almost constant, with less than 4% variation between  $\beta - 1$  at  $90^\circ$  and  $\beta - 1$  at  $30^\circ$  impact angle.

#### 5.4 Implications for the DART and Hera missions

The change in momentum caused by the DART impact will be approximated from the circular Keplerian motion of the Didymos system (Cheng et al., 2020) and therefore only the momentum transfer in the direction of the target’s orbital velocity will be measured by the

DART mission. In an ideal scenario, the DART impactor would strike Dimorphos’s surface vertically (normal incidence;  $\theta = 90$ ) in the direction of its orbital velocity. In an oblique impact, due to the asymmetric distribution of the crater ejecta, the change in momentum is not co-linear with the impactor momentum. If the DART impact occurs at a non-vertical impact angle  $\theta < 90$  then the momentum change in the orbital velocity direction can be defined as  $M\Delta v/mU = \beta \sin \theta / \cos \psi$ , which for the impact scenarios considered here can be reasonably approximated as  $M\Delta v/mU = \beta \sin \theta$ .

As seen from previous studies, the efficiency of the vertical momentum transfer produced by the DART impact,  $\beta \sin \theta$ , is very sensitive to the target properties and impact conditions (Jutzi and Michel, 2014; Stickle et al., 2015; Syal et al., 2016; Raducan et al., 2019; Raducan et al., 2020). Moreover, a number of target property configurations (e.g., different target cohesion-porosity-impact angle combinations) can result in the same deflection (Raducan et al., 2020). Therefore an observed value of  $\beta$  can be interpreted in different ways depending on the target and impact properties, which will not be known before the arrival of the Hera mission.

Having demonstrated that the analytical expressions derived here give reasonable approximations of  $\beta - 1$ , which are within 20% of the numerical data, the same methodology can then be used to extrapolate the  $\beta$  values for impacts into targets with cohesions and porosities different to those used in the oblique impact simulations presented here.

Of principal interest for the DART mission is the normal momentum transfer,  $M\Delta v/mU \approx \beta \sin \theta \cos \psi_t$ . Raducan et al. (2019) gives values for  $\mu$ ,  $C_1$  and  $k$  for DART-like vertical impacts into asteroid targets with various cohesions, porosities and internal friction coefficients. Substituting the  $\mu$ ,  $C_1$  and  $k$  constants derived from two-dimensional vertical impact simulations (Raducan et al., 2019) into Eq. (19),  $M\Delta v/mU$  can be calculated for a range of target cohesions and fixed porosity. The crater radius,  $R$ , was calculated using Eq. (2).



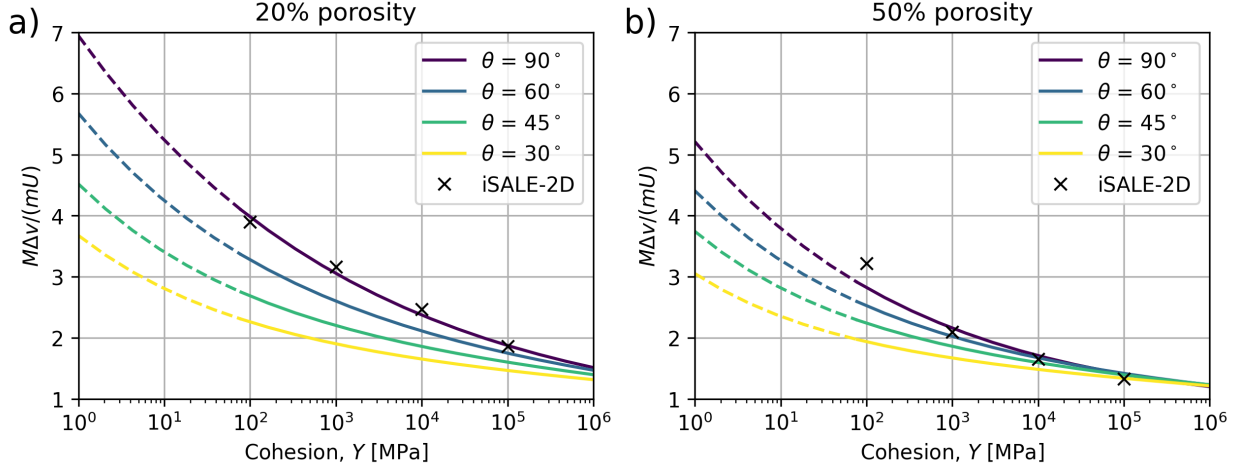


Figure 15:  $M\Delta v/mU$  trends found using Eq. (19), for oblique impacts into a 20% porous and a 50% porous target.

Figure 15 shows the analytical  $M\Delta v/mU (\approx \beta \sin \theta)$  estimates for impacts at vertical, 60°, 45° and 30°, into targets with a cohesion between 1 Pa and 1 MPa and a fixed porosity of 20% (Fig. 15a) and 50% (Fig. 15b). This analytical approximation shows that for a 100 Pa, 20% porous target, a 30° impact angle would reduce  $M\Delta v/mU$  by up to 50%. This relative difference seems to increase with decreasing cohesion. On the other hand, for a 100 Pa, 50% porous target, a 30° impact angle would reduce  $M\Delta v/mU$  by about 30%. Further impact simulations at oblique angles into targets with a range of cohesions and porosities will verify and extend the limits of applicability of these scaling relationships and quantify any associated errors.

The semi-analytical model presented in this work and shown in Figure 15 provides a framework to determine the expected  $\beta - 1$  values from an oblique impact, given known target properties and impact conditions. However this analysis can also work in reverse: from known  $\beta - 1$  values, one could determine the range of possible target properties and impact conditions. In this way, the  $\beta$  value calculated from the observed change in the asteroid's orbit can be used to determine the range of possible target properties that would produce such deflection. An advantage of this semi-empirical approach is that it avoids the need for computationally expensive numerical simulations to span a very large parameter

space, especially in three-dimensions.

In addition to the momentum transfer efficiency recorded from Earth, information about the DART crater ejecta plume will also be available and will be provided by the LICIA Cube (Cheng et al., 2020). LICIA (Light Italian Cubesat for Imaging of Asteroids) is the Italian Space Agency (ASI) contribution to the DART mission. The CubeSat will be carried by the DART spacecraft and will be released in the vicinity of the Didymos system before the impact. The main aim of the CubeSat is to take images of the ejecta plume, over a range of angle phases, at 136–163 s after the impact.

The opacity of the crater ejecta plume as a function of height above the surface and time after the impact was shown to depend on target properties and can be used as a proxy for approximating the target strength (Richardson et al., 2009; Holsapple and Housen, 2007; Cheng et al., 2020). Current analytical models of the ejecta plume (Holsapple and Housen, 2007; Cheng et al., 2020) assume that the ejected particles are launched from the impact point at a constant angle of  $45^\circ$  to the horizontal. However, this and previous work (Luther et al., 2018) has shown that the ejection angle can vary by up to  $30^\circ$  depending on the target porosity or coefficient of internal friction and with azimuth in an oblique impact. For an accurate characterisation of the target properties, this variation in ejection angle will need to be taken into account when comparing analytical models to impact ejecta plume observations.

## 6 Conclusions

The DART mission will impact Didymos’s satellite, Dimorphos, at an oblique angle, and deflect it by an amount detectable from Earth. The DART impact angle depends on the spacecraft’s trajectory and the target slope at the point of impact, which is not known prior to the impact. The ejected material from oblique impacts is highly asymmetrical early in the cratering process, and this asymmetry influences the momentum transfer. iSALE-3D simulations of DART-like impacts at oblique angles show that the vertical momentum

transfer efficiency (i.e.,  $\beta - 1$ ) is similar for different impact angles. However, the imparted momentum is reduced as the impact angle decreases. For a  $45^\circ$  oblique DART-like impact, the momentum imparted to the target is expected to be reduced by up to 70% compared to the momentum imparted from a vertical impact. Therefore, to achieve maximum deflection efficiency, it is desired that the DART spacecraft will hit Dimorphos at an angle as close to  $90^\circ$  as possible.

For the cases we simulated here, the ejected momentum is not normal to the surface and there is a small downrange component to the net target momentum vector. However, the direction of the total momentum vector is observed to ‘straighten up’ as crater growth becomes more symmetric at late times.

iSALE-2D simulations of vertical impacts show that the ejection angle of the crater ejecta is very sensitive to target properties, especially with target coefficient of internal friction, and can vary by up to  $30^\circ$ . The ejection angle influences the geometry of the DART crater ejecta cone, which will be imaged by the LICIACube.

The work presented here represents the first step towards an empirical scaling relationship for oblique impacts. This work can also be used as a framework to determine an analytical approximation of the vertical component of the ejecta momentum,  $\beta - 1$ , given known target properties. While the derived model is in good agreement with laboratory experiments, iSALE-2D and iSALE-3D simulation results, further studies are needed to determine its limits of applicability.

## 7 Acknowledgements

We gratefully acknowledge the developers of iSALE ([www.isale-code.de](http://www.isale-code.de)), including Kai Wünnemann, Dirk Elbeshausen, Boris Ivanov and Jay Melosh. This work has received funding from the UK’s Science and Technology Facilities Council (STFC) (Grant ST/S000615/1) and from the European Union’s Horizon 2020 research and innovation programme, NEO-MAPP, under grant agreement No. 870377.

## 8 Appendix

Additional supporting information (tables, model outcomes) will be archived on GitHub and provided at the time of the publication as a DOI.

## References

- Ahrens, T. J. and Cole, D. M. (1974). Shock compression and adiabatic release of lunar fines from Apollo 17. *Lunar and Planetary Science Conference Proceedings*, 3:2333.
- Amsden, A. A., Ruppel, H. M., and Hirt, C. W. (1980). SALE: a simplified ALE computer program for fluid flow at all speeds. Technical Report LA-8095, 5176006.
- Anderson, J. L. B., Schultz, P. H., and Heineck, J. T. (2003). Asymmetry of ejecta flow during oblique impacts using three-dimensional particle image velocimetry. *Journal of Geophysical Research: Planets*, 108(E8).
- Anderson, J. L. B., Schultz, P. H., and Heineck, J. T. (2004). Experimental ejection angles for oblique impacts: Implications for the subsurface flow-field. *Meteoritics & Planetary Science*, 39(2):303–320.
- Atchison, J. A., Ozimek, M. T., Kantsiper, B. L., and Cheng, A. F. (2016). Trajectory options for the DART mission. *Acta Astronautica*, 123:330–339.
- Benz, W. and Asphaug, E. (1999). Catastrophic Disruptions Revisited. *Icarus*, 142(1):5–20.
- Chapman, C. R. and McKinnon, W. B. (1986). Cratering of planetary satellites. In Burns, J. A. and Matthews, M. S., editors, *Satellites*, pages 492–580. University of Arizona Press, Tucson.
- Cheng, A. F., Michel, P., Jutzi, M., Rivkin, A. S., Stickle, A., Barnouin, O., Ernst, C., Atchison, J., Pravec, P., and Richardson, D. C. (2016). Asteroid Impact & Deflection Assessment mission: Kinetic impactor. *Planetary and Space Science*, 121:27–35.
- Cheng, A. F., Rivkin, A. S., Michel, P., Atchison, J., Barnouin, O., Benner, L., Chabot, N. L., Ernst, C., Fahnestock, E. G., Kueppers, M., Pravec, P., Rainey, E., Richardson, D. C., Stickle, A. M., and Thomas, C. (2018). AIDA DART asteroid deflection test: Planetary defense and science objectives. *Planetary and Space Science*, 157:104–115.

- Cheng, A. F., Stickle, A. M., Fahnestock, E. G., Dotto, E., Della Corte, V., Chabot, N. L., and Rivkin, A. S. (2020). DART mission determination of momentum transfer: Model of ejecta plume observations. *Icarus*, 352:113989.
- Collins, G. S., Melosh, H. J., and Ivanov, B. A. (2004). Modeling damage and deformation in impact simulations. *Meteoritics & Planetary Science*, 39(2):217–231.
- Collins, G. S., Melosh, H. J., and Wünnemann, K. (2011). Improvements to the epsilon-alpha porous compaction model for simulating impacts into high-porosity solar system objects. *International Journal of Impact Engineering*, 38(6):434–439.
- Davison, T. M., Collins, G. S., Elbeshausen, D., Wünnemann, K., and Kearsley, A. (2011). Numerical modeling of oblique hypervelocity impacts on strong ductile targets. *Meteoritics & Planetary Science*, 46(10):1510–1524.
- Elbeshausen, D. and Wünnemann, K. (2011). iSALE-3D: A three-dimensional, multi-material, multi-rheology hydrocode and its applications to large-scale geodynamic processes. volume 10, page 287–301.
- Elbeshausen, D., Wünnemann, K., and Collins, G. S. (2009). Scaling of oblique impacts in frictional targets: Implications for crater size and formation mechanisms. *Icarus*, 204(2):716–731.
- Feldhacker, J. D., Syal, M. B., Jones, B. A., Doostan, A., McMahon, J., and Scheeres, D. J. (2017). Shape dependence of the kinetic deflection of asteroids. *Journal of Guidance, Control, and Dynamics*, 40(10):2417–2431.
- Gulde, M., Kortmann, L., Ebert, M., Watson, E., Wilk, J., and Schäfer, F. (2018). Robust optical tracking of individual ejecta particles in hypervelocity impact experiments. *Meteoritics and Planetary Science*, 53(8):1696–1704.

- Hirt, C. W., Amsden, A. A., and Cook, J. L. (1974). An Arbitrary Lagrangian-Eulerian Computing Method for All Flow Speeds. *Journal of Computational Physics*, 14:227–253.
- Hoerth, T., Schäfer, F., Thoma, K., Kenkmann, T., Poelchau, M. H., Lexow, B., and Deutsch, A. (2013). Hypervelocity impacts on dry and wet sandstone: Observations of ejecta dynamics and crater growth. *Meteoritics & Planetary Science*, 48(1):23–32.
- Holsapple, K. A. and Housen, K. R. (2007). A crater and its ejecta: An interpretation of Deep Impact. *Icarus*, 191(2, Supplement):586–597.
- Holsapple, K. A. and Schmidt, R. M. (1987). Point source solutions and coupling parameters in cratering mechanics. *Journal of Geophysical Research: Solid Earth*, 92(B7):6350–6376.
- Housen, K. R. and Holsapple, K. A. (2003). Impact cratering on porous asteroids. *Icarus*, 163(1):102–119.
- Housen, K. R. and Holsapple, K. A. (2011). Ejecta from impact craters. *Icarus*, 211(1):856–875.
- Housen, K. R., Schmidt, R. M., and Holsapple, K. A. (1983). Crater ejecta scaling laws: Fundamental forms based on dimensional analysis. *Journal of Geophysical Research: Solid Earth*, 88(B3):2485–2499.
- Ivanov, B. A. and Artemieva, N. A. (2002). Numerical modeling of the formation of large impact craters. In *Special Paper 356: Catastrophic events and mass extinctions: impacts and beyond*, volume 356, pages 619–630. Geological Society of America.
- Ivanov, B. A., Deniem, D., and Neukum, G. (1997). Implementation of dynamic strength models into 2d hydrocodes: Applications for atmospheric breakup and impact cratering. *International Journal of Impact Engineering*, 20(1):411–430.
- Ivanov, B. A., Melosh, H. J., and Pierazzo, E. (2010). Basin-forming impacts: Reconnaissance modeling. *Geological Society of America Special Papers*, 465:29–49.

- Johnson, B., Bowling, J. T., and Melosh, J. (2014). Jetting during vertical impacts of spherical projectiles. *Icarus*, 238:13–22.
- Jutzi, M. and Michel, P. (2014). Hypervelocity impacts on asteroids and momentum transfer I. Numerical simulations using porous targets. *Icarus*, 229:247–253.
- Lundborg, N. (1967). The strength-size relation of granite. *International Journal of Rock Mechanics and Mining Sciences & Geomechanics Abstracts*, 4(3):269–272.
- Luther, R., Zhu, M.-H., Collins, G., and Wünnemann, K. (2018). Effect of target properties and impact velocity on ejection dynamics and ejecta deposition. *Meteoritics & Planetary Science*, 53(8):1705–1732.
- Michel, P., Cheng, A., Küppers, M., Pravec, P., Blum, J., Delbo, M., Green, S., Rosenblatt, P., Tsiganis, K., Vincent, J., Biele, J., Ciarletti, V., Hérique, A., Ulamec, S., Carnelli, I., Galvez, A., Benner, L., Naidu, S., Barnouin, O., Richardson, D., Rivkin, A., Scheirich, P., Moskovitz, N., Thirouin, A., Schwartz, S., Campo Bagatin, A., and Yu, Y. (2016). Science case for the asteroid impact mission (aim): A component of the asteroid impact & deflection assessment (aida) mission. *Advances in Space Research*, 57(12):2529 – 2547.
- Michel, P., Kueppers, M., Sierks, H., Carnelli, I., Cheng, A. F., Mellab, K., Granvik, M., Kestilä, A., Kohout, T., Muinonen, K., Näsilä, A., Penttilä, A., Tikka, T., Tortora, P., Ciarletti, V., Hérique, A., Murdoch, N., Asphaug, E., Rivkin, A., Barnouin, O., Bagatin, A. C., Pravec, P., Richardson, D. C., Schwartz, S. R., Tsiganis, K., Ulamec, S., and Karatekin, O. (2018). European component of the AIDA mission to a binary asteroid: Characterization and interpretation of the impact of the DART mission. *Advances in Space Research*, 62(8):2261–2272.
- Prieur, N. C., Rolf, T., Luther, R., Wünnemann, K., Xiao, Z., and Werner, S. C. (2017). The effect of target properties on transient crater scaling for simple craters. *Journal of Geophysical Research: Planets*, 122(8):2017JE005283.



- Raducan, S. D., Davison, T. M., and Collins, G. S. (2020). The effects of asteroid layering on ejecta mass-velocity distribution and implications for impact momentum transfer. *Planetary and Space Science*, 180:104756.
- Raducan, S. D., Davison, T. M., Luther, R., and Collins, G. S. (2019). The role of asteroid strength, porosity and internal friction in impact momentum transfer. *Icarus*, 329:282–295.
- Richardson, D. C., Michel, P., Walsh, K. J., and Flynn, K. W. (2009). Numerical simulations of asteroids modelled as gravitational aggregates with cohesion. *Planetary and Space Science*, 57(2):183–192.
- Richardson, J. E., Melosh, H. J., Lisse, C. M., and Carcich, B. (2007). A ballistics analysis of the Deep Impact ejecta plume: Determining Comet Tempel 1’s gravity, mass, and density. *Icarus*, 190(2):357–390.
- Schmidt, R. M. (1980). Meteor Crater: Energy of formation - Implications of centrifuge scaling. volume 11, pages 2099–2128.
- Schmidt, R. M. and Housen, K. R. (1987). Some recent advances in the scaling of impact and explosion cratering. *International Journal of Impact Engineering*, 5(1):543–560.
- Schultz, P. H. (1999). Ejecta Distribution from Oblique Impacts into Particulate Targets. volume 30.
- Stickle, A. M., Atchison, J. A., Barnouin, O. S., Cheng, A. F., Crawford, D. A., Ernst, C. M., Fletcher, Z., and Rivkin, A. S. (2015). Modeling Momentum Transfer from Kinetic Impacts: Implications for Redirecting Asteroids. *Procedia Engineering*, 103:577–584.
- Syal, M. B., Owen, J. M., and Miller, P. L. (2016). Deflection by kinetic impact: Sensitivity to asteroid properties. *Icarus*, 269:50–61.
- Tillotson, H. J. (1962). Metallic Equations of State for Hypervelocity Impact. *General Atomic Report*, GA-3216:141.

Wünnemann, K., Collins, G. S., and Melosh, H. J. (2006). A strain-based porosity model for use in hydrocode simulations of impacts and implications for transient crater growth in porous targets. *Icarus*, 180(2):514–527.

Yanagisawa, M. and Hasegawa, S. (2000). Momentum Transfer in Oblique Impacts: Implications for Asteroid Rotations. *Icarus*, 146(1):270–288.